The Inner Galaxy in the Infrared

Iulia Simion

21 Mars - 29 June 2011.

- Report -

Master 2 Recherche Astronomie & Astrophysique, Observatoire de Paris

This internship has been done at the Institute of Astronomy, Cambridge , under the supervision of Dr. Vasily Belokurov.

Contents

1 Introduction

Many developments have been made in the scientific study of our Galaxy since Galileo's discovery that its milk-white colour on the sky is due to the fact that it is made up of an enormous number of stars which can not be resolved with the naked eye. With time, as higher performance telescopes were built and data at new wavelengths became available, our knowledge of the Milky Way's structure increased rapidly and we are able today to build models which describe analytically its stellar content. However, until recently, models described a smooth Galaxy, with four distinct components: the bulge, the thin and thick disks, and the stellar halo (Gilmore & Reid 1983). In the classical scenario, the origin of our Galaxy is described by a rapid radial collapse of a protogalactic cloud, followed by a rapid settling of gas into a dynamically cold, centrifugally supported disk where stars form (Eggen et al. 1962). Another group of stars can be distinguished, which relies less on rotation and is distributed in a thick disk. This model explained in an easy way the properties of the stellar populations known at the time: low metallicity Population II stars formed during the initial collapse and populated the halo while younger Population I stars and intermediate Population II stars formed after the gas settled into the Galactic plane and populated the disks (Baade 1944).

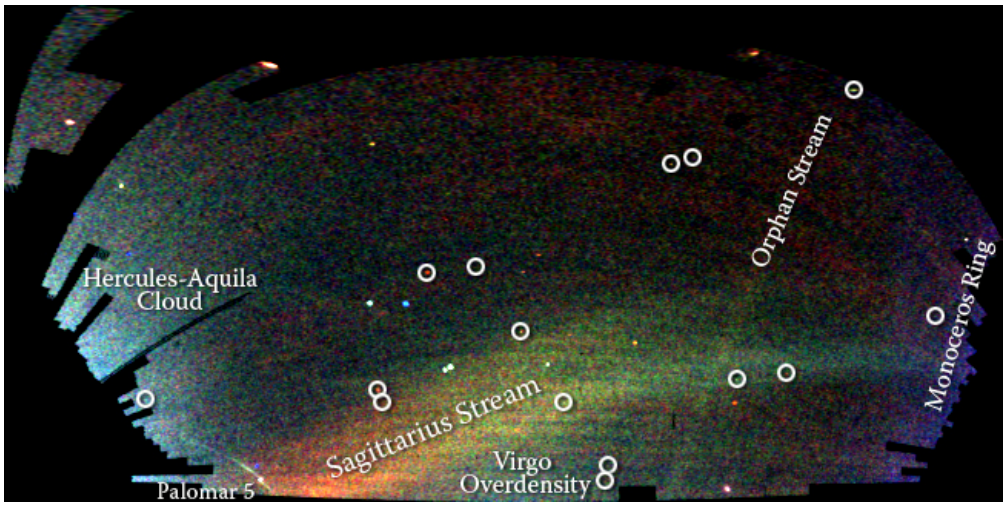

Figure 1: Spatial density of SDSS stars with $g - r < 0.4$ around the north Galactic cap in equatorial coordinates. The plot is an RGB composite with blue for the most nearby stars with $20.0 < r < 20.66$, green for stars with $20.66 < r < 21.33$ and red for the most distant stars with $21.33 < r < 22.00$. Marked with circles are some of the globular clusters.

The observed distribution of stars in the thin and the thick disk is described analytically by a double exponential law, each component of the disk having different characteristic scale heights and scale lengths (Soneira 1980, [5] Gilmore et al. 1989). This distribution, function of distance, is predicted to be smooth and be perturbed just locally by bursts of star formation or Galactic spiral arms. In recent years, stellar counts from the Palomar Observatory Sky Survey, 2MASS, UKIDSS (in low latitude regions) and the Sloan Digital Sky Survey, have shown that the structure of our Galaxy is more complex. In fact, numerous substructures have been discovered in the distribution and kinematics of stars in our Galaxy. These discoveries include the Sgr dwarf tidal stream in the halo ([8] Newberg et al. 2003), the Monoceros Ring close to the galactic plane (Newberg et al 2002, Yanny et al 2003), the Canis Major overdensity ([7]

Marin et al. 2004), the Triangulum Andromeda overdensity ([10] Rocha-Pinto et al. 2004), the Orphan stream ([4] Belokurov et al. 2007) and the Hercules-Aquila cloud ([3] Belokurov et al. 2007). Figure 1 shows these overdensities for SDSS stars.

Much controversy surrounds the nature and origin of low galactic structures, such as the Hercules Aquila Cloud, the feature we plan to analyse in this project. Some authors argue that they represent debris from one or more recently accreted sattelites on eccentric, nearly coplanar orbits encountering the inner Galaxy ([9] Penarrubia et al 2005, Johnston et al 2008); others claim that they represent spiral arms or warped/flared regions of the Milky Way outer disk (Momany et al 2004). In fact, it has been suggested that the HAC could be a large bar of the Milky Way, because of its shape on the sky. Alternatively, simulations of low inclination mergers show caustics and shells that appear similar in aspect to the HAC ([1] Villalobos et al. 2009). Discriminating between theories for the origin of these structures requires a detailed knowledge of the intrinsic populations and structure of the Milky Way disk.

The observed overdensities seem to be in good agreement with some hierchical formation models of the disk according to which accretion events (mergers or satellites) have played a major role. In these models, the age and metallicity distributions of the stars constrain the epoch and duration of disk assembly ([2] Abadi et al. 2003) as accreted dwarf sattelites are not expected to possess the same mixture of stellar populations as the outer disk of a large spiral galaxy; moreover, multiple satellite accretions would not be expected to possess identical stellar populations.

In this project, we aim to better characterize the recently discovered overdensity, the Hercules-Aquila cloud (HAC), by combining infrared photometry at low galactic latitudes with the SDSS data. Before detailed modelling can commence the properties of the HAC must be constrained, i.e. its extent, kinematics and stellar density. Understanding its origin it could also help us justify the existance of other structures such as the Virgo overdensity. The HAC is an interesting overdensity since it subtends a large extent on the sky ($\Delta l = 80°$ and b up to ± 50), it is very asymmetric accross the Galactic plane and it is offset from the galactic center. Its metal poor population is visible in the RR Lyrae distribution.

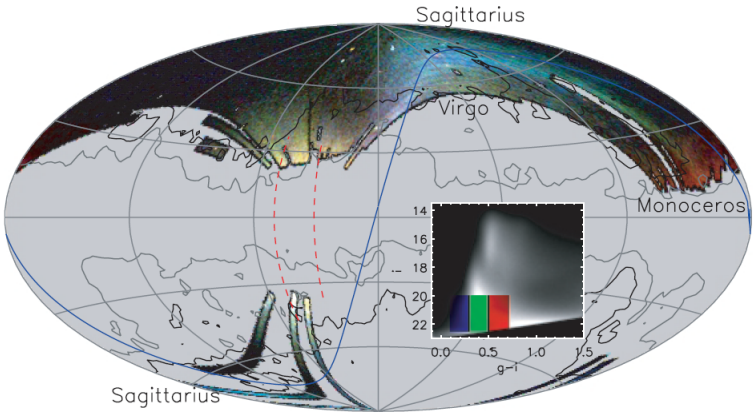

Figure 2: Areal density of SDSS stars with $0.1 < g-i < 0.7$ and $20 < i < 22.5$ in Galactic coordinates. The plot is an RGB composite with blue representing $0.1 < g - i < 0.3$, green $0.3 < g - i < 0.5$ and red $0.5 < g - i < 0.7$. We can see the arch of Sagittarius stream, and the Orphan stream in blue and multiple wraps of the Monoceros ring in red. The yellow-colored structure visible in both hemispheres is the Hercules Aquila Cloud.

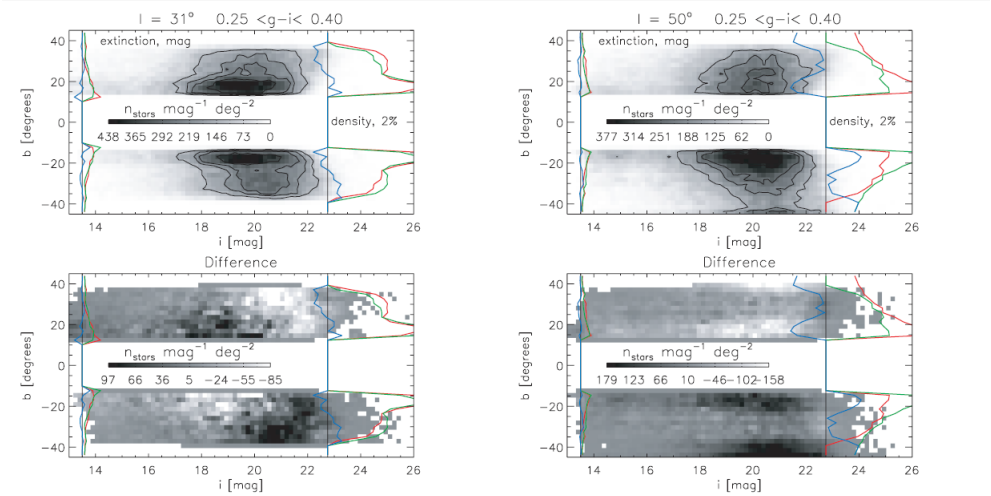

Figure 3: The top panels show the gray scale contours of the spatial density of SDSS stars in two slices at longitudes $l = 31°$ and $l = 50°$. The southermost overdensity is due to the Sagittarius stream and the main enhancement is due to the Hercules Aquila cloud which can be seen in the subtraction of densities in the two hemispheres. The HAC is situated at $l = 31°, b \approx 20°, i = 19$ mag and $l = 50°, b = -15°, i = 20$, meaning that at $l = 31°$ is closer to the Sun than at $l = 50°$. Black represents a relative overdensity to the other hemisphere and white an underdensity.

Figure 2 shows an areal density of SDSS stars with $20 < i < 22.5$, in galactic coordinates. The colours on the plot represent a colour selection of stars (Belokurov et al. 2007). The structures we can see are the Sagittarius and Orphan streams in blue, and the Monoceros ring in red. The yellow coloured structure that is visible in both hemispheres , and centered at $l = 40°$ is the Hercules Aquila Cloud.
The HAC is also visible in figure 3 where the star densities of halo stars ($0.25 < g - i < 0.4$) in the northern and southern hemispheres are compared. An estimated absolute magnitude of $M_V = -13$ has been calculated for this overdensity by comparison with the color magnitude diagram of a metal poor cluster M92 [3].
SDSS data is compromised at low latitudes due to extinction and crowding effects so the peak of the overdensity has yet to be established; as the SDSS data has already provided an indication of the stellar content of this feature, in this project we will analyze the Hercules-Aquila cloud in only two bands, J and K. The data is described in section 4.

This project is part of my Master's degree, *Astronomy & Astrophysics*, at the Observatoire Paris-Meudon in Paris.

2 Generalities

2.1 Colour magnitude diagrams

The Hertzsprung-Russell diagram (HR-diagram), developed independently by E. Hertzsprung in 1911 and H. N. Russell in 1913, represents a major step towards the understanding of stellar evolution. The HR diagram is a scatter graph of stars showing the relationship between the stars' absolute magnitudes or luminosities versus their spectral types and effective temperatures. The original diagram displayed the spectral type of stars on the horizontal axis and the absolute

magnitude on the vertical axis. Observationally, the spectral types (which are difficult to plot as they are not numerical quantities) are replaced by the color index of the stars. This type of diagram is what is often called a color-magnitude diagram (CMD) and usually it is a plot of a colour versus a magnitude, either absolute (for stars of known distance) or apparent (if the stars are at the same distance, e.g. in a cluster). In figure 4 we show an example of such a diagram [12] where each point represents a star of known distance and the colours in the diagram indicate the age range of the stars. As the stars of a given spectral MK class have a unique colour (see table II in the Appendix), the CMD is equivalent to the HR-diagram.
Another form of the diagram plots the effective surface temperature of the star on one axis and the luminosity of the star on the other. Empirical transformations between various color indices and effective temperature are also available in literature (see table I).

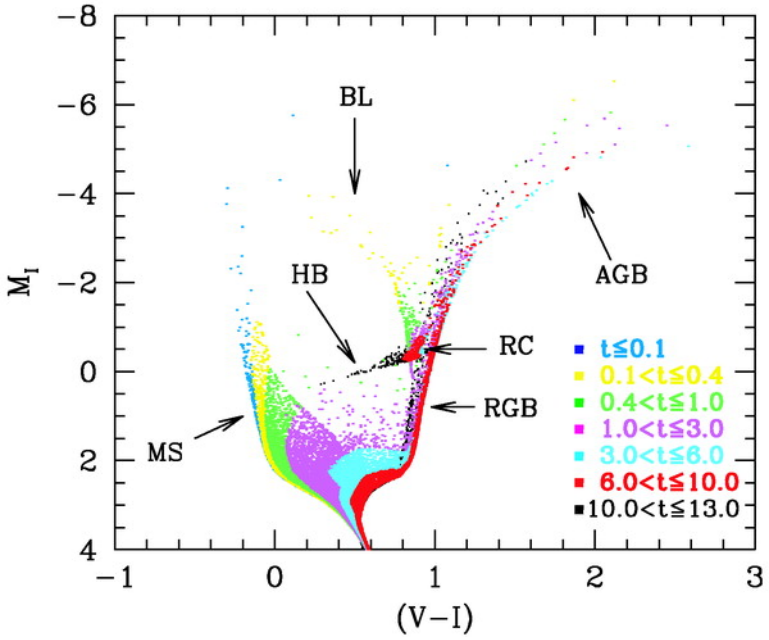

Figure 4: Color Magntitude Diagram.

The stars are not scattered at random in a CMD, as shown in figure 4. Most of the stars occupy the region in the diagram along the line called the main sequence (luminosity class V, table II in the Appendix), which also continues at faint magnitudes, and stretches from luminous hot, blue stars O to faint, cool, red M stars. The subgiant branch (SGB) joins the main sequence at $M_I \approx 2$ and stretches horizontally up to to $B - I = 0.9$ where the distribution of stars turns upwards at a luminosity much brighter than MS stars of the same type: these stars are the red giants and correspond to the luminosity class III (see table III).
The stars in figure 4 do not all have the same age. The stars of a population of age 0 would form a narrow main-sequence, called the zero-age main sequence (ZAMS).
Let us now describe briefly what happens in the different regions of the CM according to the theory of stellar structure. On the main sequence, stars are burning hydrogen to helium in their cores. This is the longest period in a star's life. The position the stars occupy on the main sequence depends on their mass, more massive stars lie up and to the left of less massive ones. When the most massive stars leave the MS they die in supernova explosions. When stars with $M < 8M_\odot$ leave the main sequence they start moving almost vertically on the red giant branch

where they spend a few years; this branch is occupied by H shell burning stars. In figure 4 we can see a concentration of stars known as the horizontal branch (HB) on which stars burn He in their cores. In metal rich clusters or in the solar neighborhood, stars form a clump at the red end of the HB called the red clump (RC). Almost vertically in the CMD, there is a region within which stars pulsate, called the instability strip. At the intersection of the evolutionary tracks of high mass stars with this strip we find the Cepheid variables and at its intersection with the HB of metal poor stars we find the RR Lyrae variables.
After leaving the HB, low mass stars in the last phases of their life start moving on the asymptotic giant branch (AGB) where they burn He in their shell. The AGB runs parallel to the RGB but is shifted slightly to the blue. When stars get to high luminosities, they start losing mass faster and eventually they return all their mass to the interstellar medium and they die.
The H-R diagram can be used to match theoretical predictions of stellar evolution models with observations of actual stars. The H-R diagram can also be used to roughly measure distances of stellar populations (or clusters) that we consider at the same distance from Earth. This can be done by comparing the apparent magnitudes of the stars in the population (usually clusters) to the absolute magnitudes of stars with known distances (or of model stars). The model is then shifted in the vertical direction, until the two main sequences overlap. The difference in magnitude that was bridged in order to match the two groups is called the distance modulus and is a direct measure for the distance (see Appendix A). We will use this technique in the next sections.

2.2 Metallicity

The metallicity (Z) of an astronomical object is the proportion of its matter made up of chemical elements other than hydrogen and helium. In the Sun, the abundances by number of various elements relative to hydrogen are roughly: helium, 0.10; carbon, 3×10^{-4}; nitrogen, 1×10^{-4}; oxygen, 6×10^{-4}; neon, 1×10^{-4}; magnesium, 3×10^{-5} and iron 4×10^{-5}.
The iron abundance in a star is calculated using:

$$[Fe/H] = log_{10}\left(\frac{n(Fe)}{n(H)}\right)_{star} - log_{10}\left(\frac{n(Fe)}{n(H)}\right)_{\odot} \tag{1}$$

and the abundance of any other metal M is:

$$[M/H] = log_{10}\left(\frac{n(M)}{n(H)}\right)_{star} - log_{10}\left(\frac{n(M)}{n(H)}\right)_{\odot}. \tag{2}$$

Often the parameters (X, Y, Z) are used; they indicate the fractional abundances by weight of hydrogen, helium, and all the metals respectively. For the Sun X=0.70, Y=0.28 and Z=0.02.
In order to investigate the relative importance of different enrichment mechanisms at various times and places Edvardsson et al. defined the quantity:

$$[\alpha/Fe] = \frac{1}{4}\big([Mg/Fe] + [Si/Fe] + [Ca/Fe] + [Ti/Fe]\big) \tag{3}$$

In general, stars that are poor in Fe are poor also in other metals; moreover, old stars have large values of $[\alpha/Fe] \approx 0.25$ while young stars have $[\alpha/Fe] \approx 0.0$. The interpretation for this is that the old stars have formed in the early life of the Milky Way when star formation was high and many of them formed in an interstellar medium that has been heavily polluted by massive supernovae. The bulge of our Galaxy shows overabundances of α elements with respect

to iron in most of its stars due to the fast evolutionary time scales.
As mentioned in the introduction, stellar populations were initially categorized as I and II. Population I, or metal-rich stars, are those young stars whose metallicity is the highest and are common in the spiral arms of the Milky Way galaxy. The Sun is considered a metal-rich star. The youngest stars, the extreme Population I, are found the closest to the Galactic plane and intermediate Population I stars are found farther out, etc. Population I stars have regular elliptical orbits around the galactic centre, with a low relative velocity. Population II contains metal-poor and old stars, which are mainly found in the galactic halo. Globular clusters also contain high numbers of Population II stars. The maximum halo metallicity is $[Fe/H] \approx -1.0$ [13], as suggested by the kinematics of stars, and it marks the transition between halo and disk metallicity even though there seems to exist an overlap of halo and disk stars in the range -1.6 and -1.0 [13] Matteucci, 1992.
It is important to know the chemical evolution of stellar populations when computing galaxy formation and evolution models. Researchers refine the models of galactic chemical evolution by combining kinematics and elemental abundances of local dwarfs; moreover, to improve these models the ages of the stars must be taken into account. Many studies have shown that there is a clear relation between age and metallicity of disk stars in the solar neighborhood (Rocha Pinto et al 2000, Meusinger et al. 1991) but others have shown that there is no evidence for age-metallicity relations as they can be created by selection effects (Feltzing et al 2001). In general, we consider that the thick disk has a mean metallicity of -0.6 dex (Wyse & Gilmore 1995) and an age of 8-12 Gyrs while the thin disk has a mean metallicity of -0.1 dex (Gilmore & Reid 1983) and an age of 1-10 Gyrs.

3 Isochrones

In order to interpret the observed CMD of stellar populations we can often use what we learn from observed CM diagrams of globular clusters, for which we assume that all the stars were born at the same epoch. Theoretical CM diagrams will help us interpret stellar populations. To build them, we first have to choose Y and Z and calculate the initial position on the ZAMS. Secondly, we let the population evolve in time by solving stellar structure equations for each star. For each step, luminosities and colours are calculated for all the stars in the population. The curve connecting all the stars in the color magnitude diagram is called an isochrone, as it represents the properties of the stellar population when all stars have the same age.
Many calculations of families of isochrones have been performed (Berg & Bell 1995, Bertelli et al. 1994, Chaboyer et al 1995, Girardi et al. 2002).
To decide which set of isochrones we will use in the next sections, we have selected a series of isochrones from the Dartmouth and Padova stellar evolution databases. The Dartmouth group provides isochrones computed for the UBVRI+2MASS photometric systems (Dotter et al. 2008). The filter transmission curves for the UBVRI photometric system (Bessel et al. 1990) were combined with 2MASS JHK filters, J (1.25 microns), H (1.65 microns), and K (2.17 microns)(Cohen et al. 2003) in order to create a set of isochrones suitable for ground based photometry from the UV to the IR. The 2MASS magnitudes were calibrated by setting the magnitudes of Vega to zero in each filter (Cohen et al 2003). The following color equations are used to calibrate the WFCAM (the WFCAM is the wide field infrared camera used to acquire the data we will analyze in this report) instrumental magnitudes in the 2Mass photometric

system:

$$J_{wfcam} = J - 0.10(J - K)$$
$$H_{wfcam} = H + 0.15(J - H)$$
$$K_{wfcam} = K - 0.05(J - K)$$

As we will make use of J_{wfcam} and K_{wfcam} magnitudes and the Dartmouth group uses the JHK photometric system for 2MASS, we had to use these equation to obtain isochrones in the WFCAM calibrated bands.
From the Padova stellar evolution database we have taken the isochrones computed by Marigo et al. 2008, with Girardi et al. 2010 for the UKIDSS ZYJHK (Vegamag) system and an initial mass function computed by Chabrier 2001. The Padova isochrones have been computed also for the JHK system we use. The Vega (αLyr) star was used for calibration; it has V=0.3 mag and all the colours are set equal to zero.

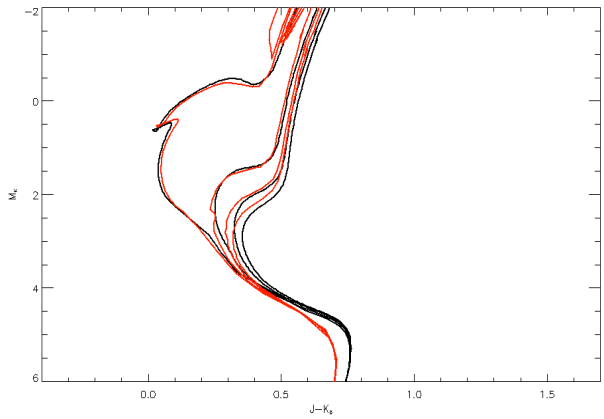

Figure 5: Isochrones at [Fe/H] $\sim$ -0.49 and ages of 1, 5, 10 and 13.5 Gyrs (age is increasing from left to right). Padova isochrones (in red) are cooler than the Darthmouth isochrone at 1Gyrs but warmer on the older isochrones, around the main sequence turnoff. A better agreement exists along the giant branch except at 13.5 Gyrs. The Padova isochrones show the AGB but the Dartmouth ones do not.

In figure 5 we show the Padova and Dartmouth isochrones, for comparison. The isochrones have a metallicity of [Fe/H] $\sim$ -0.49 and ages of 1, 5, 10 and 13.5 Gyrs (age is increasing from left to right). Padova isochrones (in red) are cooler than the Darthmouth isochrone at 1Gyrs but warmer than the older isochrones, around the main sequence turnoff. A better agreement exists along the giant branch except at 13.5 Gyrs. The Padova isochrones show the AGB but the Dartmouth ones do not. For the Padova isochrones we cannot choose the helium abundances and this may produce the significant differences we see between the two sets of isochrones. In fact, changing Y from Y=0.2 to Y=0.3 shifts the MS downwards by 0.2 mag and makes the SGB steeper. We think this produces the main difference (Binney & Merrifield). Increasing Z, the isochrones shift to the right of the CMD and the shape of the SGB changes. This is due to the line blanketing effects of heavy elements, which suppress the emission of blue light by metal rich stars.
In figure 6 we show four sets of isochrones of ages 1, 5, 10, 13.5 Gyrs, the colour is indicating the metallicity. We also show the isochrones for the same ages and metallicity in figure 6 but for [α/Fe]=0.00 and [α/Fe]=0.40. The difference $J-K$ increases with [α/Fe], but the difference

is smaller for the 1Gyr isochrones. Moreover, as the metallicity decreases, the color differences due to variations in [α/Fe] decrease (Cassini et al.2004).

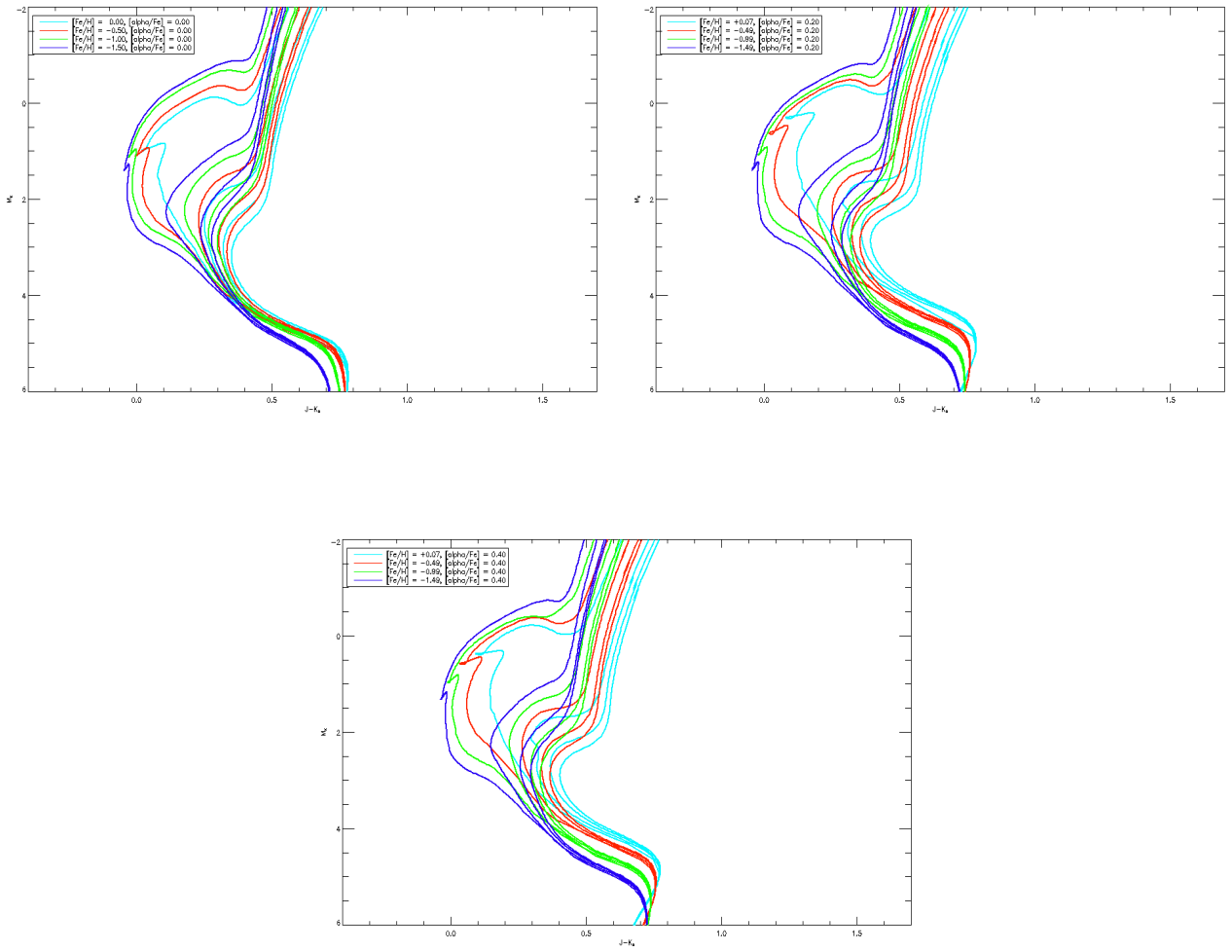

Figure 6: Set of isochrones of ages 1, 5, 10, 13.5 Gyrs with [α/Fe]=0.00, [α/Fe]=0.20 [α/Fe]=0.40 computed by the Padova group. Ages (same colour) and metallicities (different colour) increase from left to right. The difference $J-K$ increases with [α/Fe], but the difference is smaller for the 1Gyr isochrones. Moreover, as the metallicity decreases, the color differences due to variations in [α/Fe] decrease

In these graphs it can be observed that the isochrones of metal-poor populations lie below and to the left of the MS of a metal-rich one.
In the next section we will use just the Dartmouth isochrones, for comodity.

4 DATA

4.1 SDSS

The Sloan Digital Sky Survey imaging data are produced in five photometric bands *u, g, r, i* and *z* (e.g. Fukugita et al. 1996; Gunn et al. 2006). The data is automatically processed though pipelines to measure astrometric and photometric properties (e.g. Lupton et al. 1999, Stoughton et al. 2002). In this project we have used Data Release 8/SDSS data in a strip centered at $l = 50°$ and 2° wide, running from positive to negative latitudes $b = |28|°$ as shown in figure 11.
All the photometric data are dereddened using the maps of Schlegel et al 1998 [11]. The extinction correction is not perfect and this is due to the fact that these maps are just correct within 10% or better. Moreover, the Schlegel maps do not provide the wavelength dependence of the interstellar correction. For the extinction corrections in the five SDSS photometric bands and UKIRT JHK bands we use the conversion coefficients derived for an $R_V = A_V/E(B-V) = 3.1$ dust model (e.g. Snedden et al. 1978).

4.2 UKIRT

We dispose of a series of JK-only tiles (0.75 sq deg) in two strips ($l = 31°, l = 50°$) that overlie the Hercules Aquila structure. The strips extend in latitude from $b = -25°$ to $+25\circ$ as shown in figure 7. The field at $l = 50°, b = -30°$ is clearly damaged so we exclude it from our analysis. We have applied full Schlegel extinction correction to all stars in the every field. This may lead to an over-correction of interstellar extinction for the nearest stars because they are not behind all the dust.

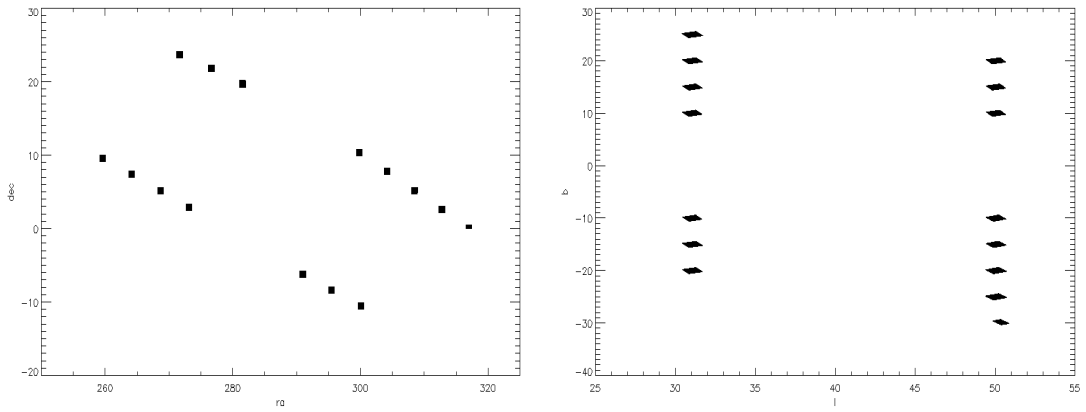

Figure 7: *left*: Right ascension vs declination of our data in Equatorial coordinates. *right*: Longitude vs latitude of the UKIRT data in Galactic coordinates. We observe that the stripe at $l = 50°, b = -30°$ is damaged.

5 UKIRT: Data analysis

5.1 CMDs

The first step in understanding the stellar populations we are observing is to construct color magnitude diagrams for the stellar classified objects, on each line of sight (figure 7). In figure 8 we show a $J-K$ vs. K color magnitude diagram, for the field $l = 31°, b = 10°$ while in the Appendix C we show the rest of the CMDs.

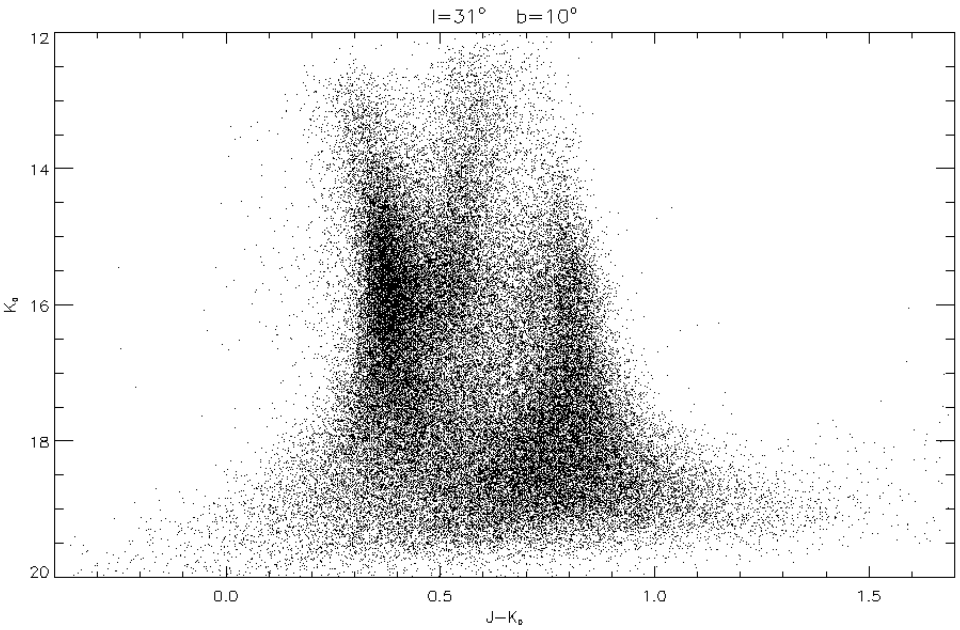

Figure 8: J-K vs K colour magnitude diagram for the field $l = 31°, b = 10°$. ()

At first sight we can already notice that stars are not distributed randomly in the diagram: we can distinguish a first concentration of stars at $0.3 < J-K < 0.4$, a second one at $0.4 < J-K < 0.65$ for $12 < K < 16.5$ and a third one at fainter magnitudes, for $0.7 < J-K < 0.9$. In this chapter we will focus on characterizing these populations by finding their age, metallicity, distance and their location in the disk (thin disk or thick disk). From tables II and III we can already see that the stars at $0.3 < J-K < 0.4$ are FG stars (MK spectral type), the ones at $0.4 < J-K < 0.65$ are GK stars that belong to the luminosity class V (main sequence) or III (giants) and at $0.7 < J-K < 0.9$ there are the cooler and fainter KM stars. At the $0.1 < J-K < 0.3$ colour we can see a few stars at high magnitudes. As they are at the blue end of the CMD and are isolated from the main distribution of stars, we think that these stars are white dwarfs that belong to the thin disk and are close to us.
We assume the second population contains giant branch stars (see fig. 4) and, by observing the full set of CMDs shown in the Appendix, we can notice it is symmetric with respect to the galactic plane, $b = 0°$. To test it, we build a box (figure 9) on the giant branch with $14 < K < 16.3$ and $0.44 < J-K < 0.62$ ensuring to avoid contamination from the first concentration of stars. We count the number of stars (N) in this box for each field and in figure 10 we show their distribution (b vs N) for the two longitudes. Assuming Poissonian errors on the counts, the best fit would give for the center of the peak, b_0, negative values: $b_0 = -0.40 \pm 0.05$ at $l = 31°$ and $b = -0.38 \pm 0.06$ at $l = 50°$, showing that we count more stars

at negative latitudes. Forcing the gaussian to be centered on $b_0 = 0$, we can easier observe the underdensities of stars at positive latitudes (figure 10).

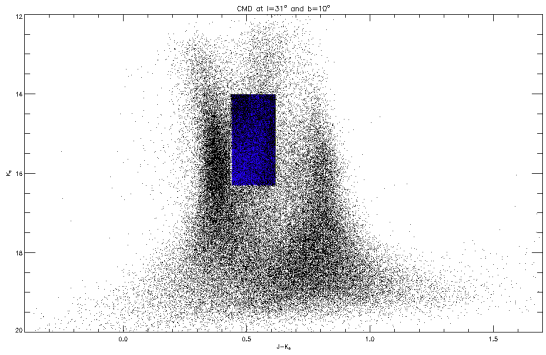

Figure 9: Star counts.

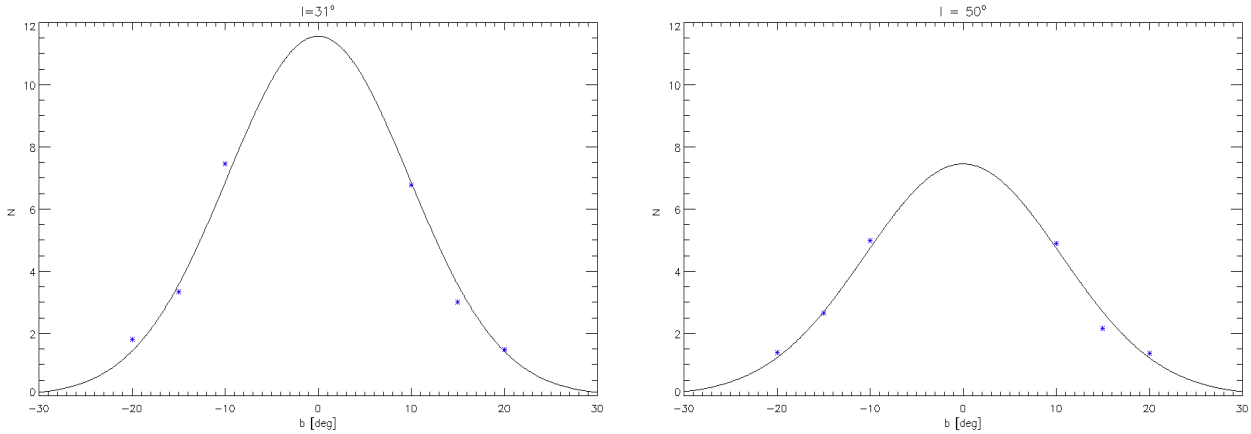

Figure 10: Gaussian fit. We observe an overdensity at $b = -15°$ and at $b = -10°$ for $l = 31°$ with $N = 7470 \pm 86$ and $N = 3341 \pm 58$ respectively, to be compared with $N = 6777 \pm 82$ and $N = 3018 \pm 55$ at positive altitudes. Also at $b = -20°$ there is a slight overdensity with N $= 1801 \pm 42$ to be compared with $N = 1490 \pm 39$. At $l = 50°$ there seems to be a strong underdensity at $l = 15°$ where we count $N = 2175 \pm 47$ much less than $N = 2666 \pm 52$ the value at $b = -10°$. The N values are given in thousands.

As mentioned in the introduction, the structure we are interested in, the Hercules Aquila Cloud, is seen at $l = 31°, b \approx 20°, i = 19$ mag and $l = 50°, b = -15°, i = 20$ mag for the colours $0.25 < g - i < 0.40$. For comparison, we would like to know where we should find it in our colour magnitude diagrams. To do so, we find the close matches between the UKIRT stars and the SDSS DR8 stars by their position on the sky. Once we have found the same stars in the SDSS and UKIRT fields, we can find a relation between the $J - K$ and $g - i$ colours. In figure 11 we show the $l = 50°$ SDSS strip in black and the UKIRT strips in blue. Performing a linear fit (fig. 12) between colours of the matches of the two data sets, we find five relations for the five different fields ($l = 50°, b = |15|°, b = |20|°, b = -25°$) we have close matched that indicate that to the $0.25 < g - i < 0.40$ colour corresponds the $0.20 < J - K < 0.40$ colour, which is situated at the blue end of our CMDs.

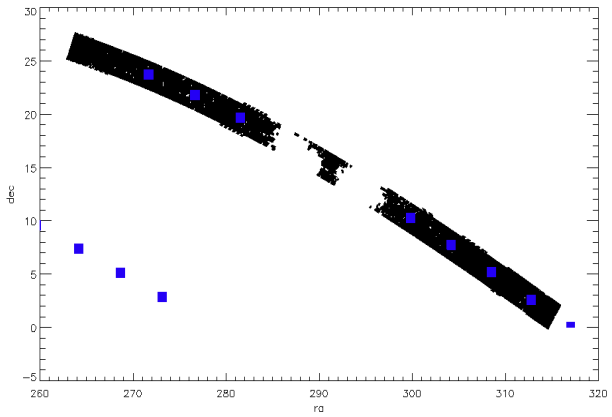

Figure 11: $l = 50°$ strip for the SDSS data in black and overlaid the UKIRT data at the same longitude in blue. We close matched the 2 data sets for all the UKIRT tiles, except for the ones at $b = 10°$.

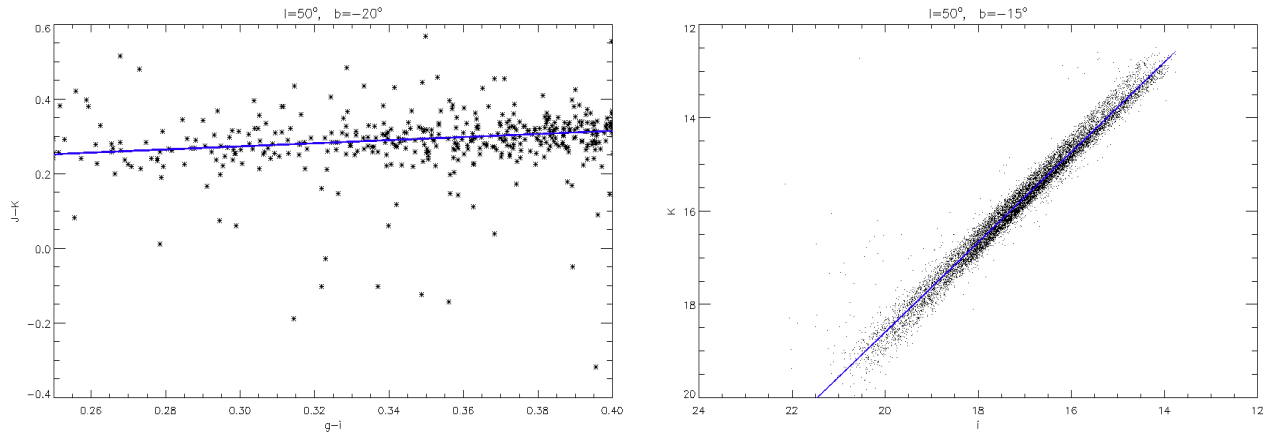

Figure 12: *left*: Linear fit showing the close matches between the SDSS stars and the UKIRT stars. We can graphically see that to the $0.25 < g - i < 0.40$ colour corresponds roughly a $0.0 < J - K < 0.4$ colour. *right*: i vs K.

In order to identify the apparent magnitude K at which we should find the Hercules-Aquila cloud, we find a linear relation between i and K (second order and third order polynomial interpolations do not give significantly different values) as shown in fig. 12. We find five different relations for five fields in the $l = 50°$ strip; for example, matches at $b = 50°, l = 15°$ and $b = 50°, l = -15°$ give the relations $K = -0.70 + 0.96i$ and $K = -0.69 + 0.96i$ respectively. Considering the average value we obtain for K in every field, at $i = 19$ mag, $i = 20$ mag and $i = 21$ mag we will correspond $K = 17.6 \pm 0.05$ mag, $K = 18.6 \pm 0.05$ and $K = 19.5 \pm 0.05$. In conclusion, if we look at fig. 8 we notice that the HAC should be found at low magnitudes and blue colours. It is important at this point to mention that the errors at the faint magnitudes we are interested in are very large (fig. 13) meaning we will not be able to do an accurate analysis of the HAC with the present UKIRT data. Another problem is the data incompleteness: in the fields $b = 31°, l = -20°$ and $b = 50°, l = 20°$ shown in the Appendix C, the data at faint K magnitudes is missing. To test that it is actually a problem with the data and it is not due to a real lack of stars in this region, we plotted also the non stellar objects (galaxies mainly) in all the fields: we observed that non-stellar objects are absent at faint magnitudes in the same fields as the stellar objects (e.g. fig. 42 in the Appendix C).

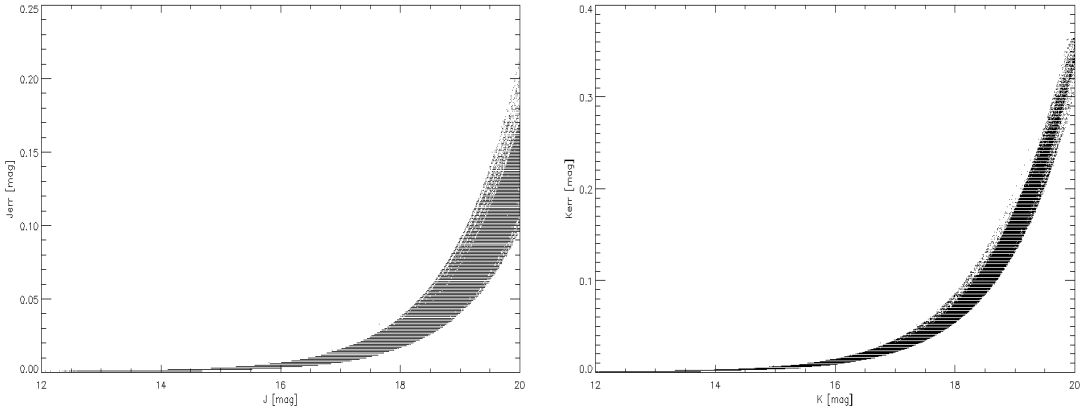

Figure 13: Errors on the apparent magnitudes J and K. Errors increase at faint magnitudes due to photon noise.

5.2 Characteristics of the populations observed

If the assumed metallicity and age are correct, the isochrones should overlay well on the CMDs of the populations we observe. To identify the metallicity and age of our stellar population, we will need to use the isochrones, described in section 3.

In figure 14, 4 sets of isochrones with different metallicity are shown (see also figure 6). For each metallicity, identified by a different colour, four ages have been chosen: 1, 5, 10, 13.5 Gyrs (from left to right). Very easily it can be noticed that the young isochrones, of 1 and 5 Gyrs, do not overlay on our data. The few scattered stars observed at the very blue end of the CMDs are white dwarfs that are very near to us. We observe that more metal rich and older isochrones seem to perform better. As we are looking inside the galaxy, almost in the bulge direction, it is reasonable to exclude metal poor populations, such as [Fe/H] $= -1.49$. Also, in this direction the stars can be old, so an estimate of 10Gyrs is a good approximation. The old isochrones at [Fe/H] $= 0.00$ overlay well on our population in the main sequence and turn off stars but they are too steep for the GB.

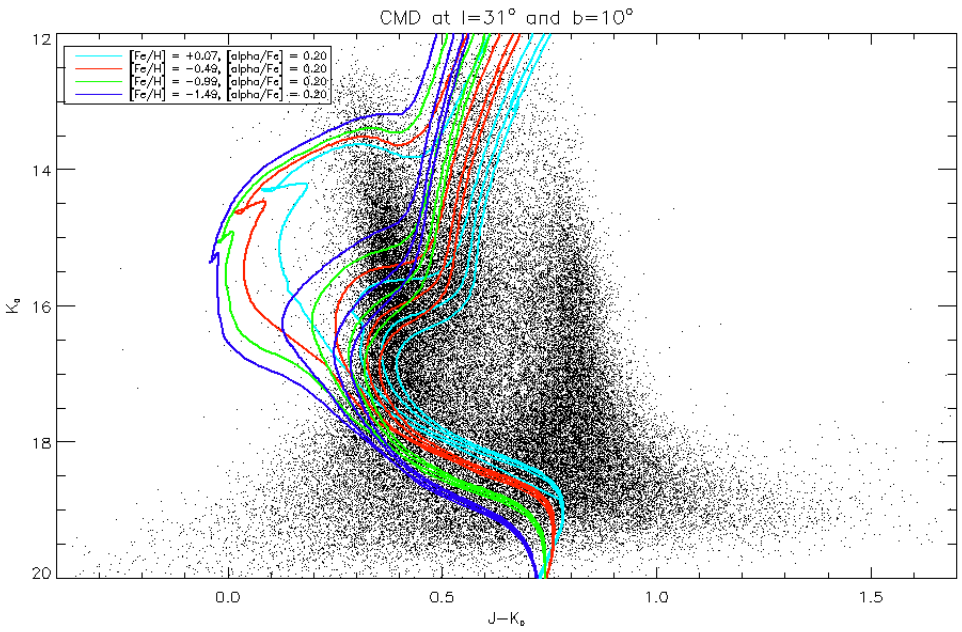

Figure 14: 4 sets of isochrones with different metallicity are shown. For each metallicity, identified by a different colour, 4 different ages have been chosen: 1, 5, 10, 13.5 Gyrs (from left to right) with a modulus distance of 14 (left).

The first concentration of stars, at color 0.3-0.4 are main sequence stars of the thick disk scattered along the line of sight. The faintest stars are the farthest and the most luminous the closest. The second population stars are red giants while the last population stars are white dwarfs stars belonging to the thin disk which are close to us.

5.3 Hess diagrams

Hess diagrams are plots of density occurrence of stars at differing color-magnitude positions for a color magnitude diagram. They are very useful because they allow us to compare quantitatively the populations we observe in the different fields. The following Hess diagrams were constructed using bins of 0.04 on colour and of 0.1 mag on magnitude.

Before proceding, we should have a look at the double exponential model for the star counts in the disk (we will discuss it more in detail in the next section) in order to know what to expect when interpreting the Hess diagrams:

$$N \propto D^2 e^{-|R|/R_0} e^{-|Z+Z_\odot|/H} \tag{4}$$

In figure 22 we show the prediction for the star density at $b = 10°$ (black for $l = 31°$ and blue for $l = 50°$) and at $b = -10°$ (red for $l = 31°$ and green for $l = 50°$). For the thick disk we have adopted H = 900pc and scale length $R_0 = 3600$pc and for the thin disk H = 300pc and a scale length $R_0 = 2600$pc. The model predicts that N is larger at negative latitudes than at positive latitudes due to position of the Sun above the Galactic plane, which we consider to be 25pc. The model also predicts dramatic differences in the star counts between $l = 31°$ and $l = 50°$. At higher latitudes, as we get farther from the Galactic plane, we will expect less

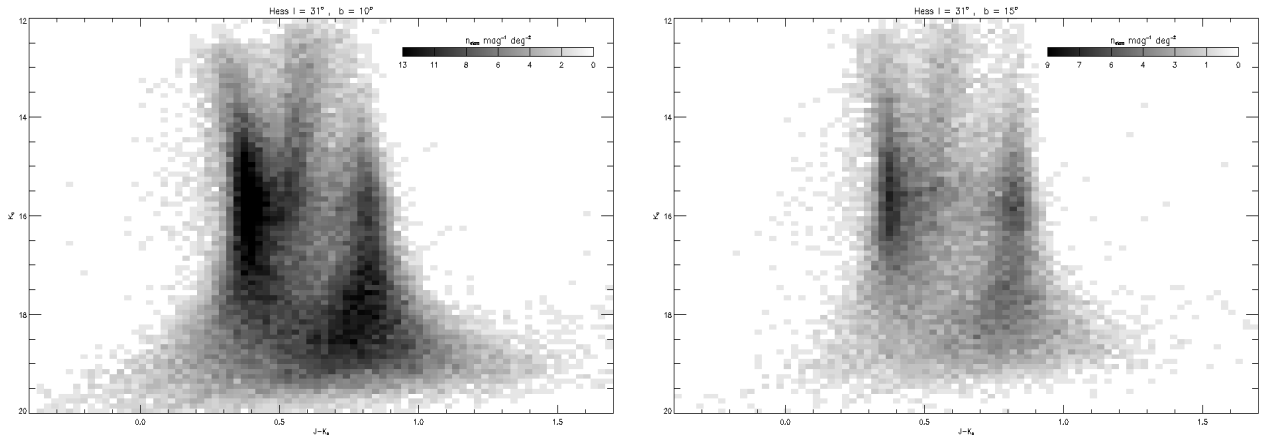

Figure 15: Hess diagrams at $l = 31°, b = 10°$ and $l = 31°, b = 15°$.

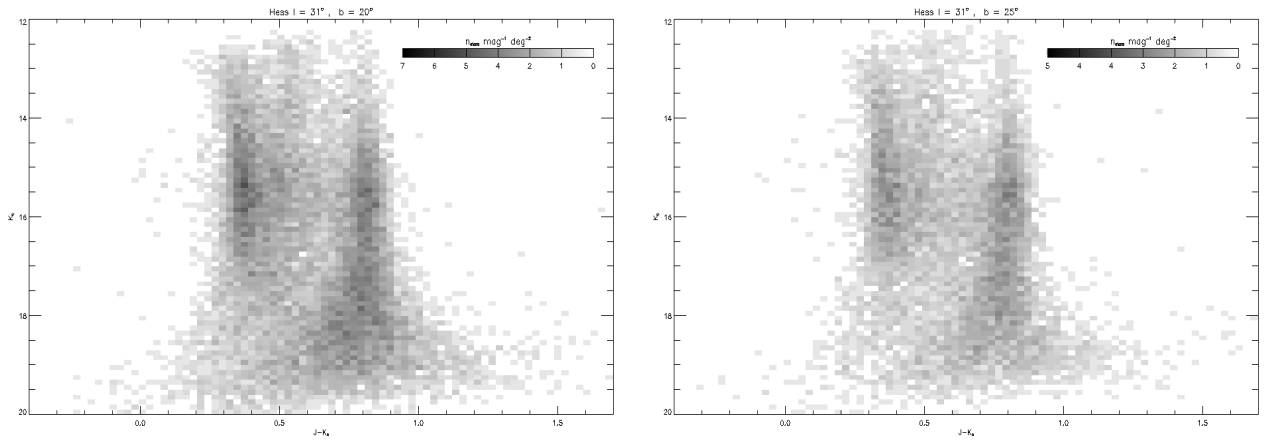

Figure 16: Hess diagrams at $l = 31°, b = 20°$ and $l = 31°, b = 25°$.

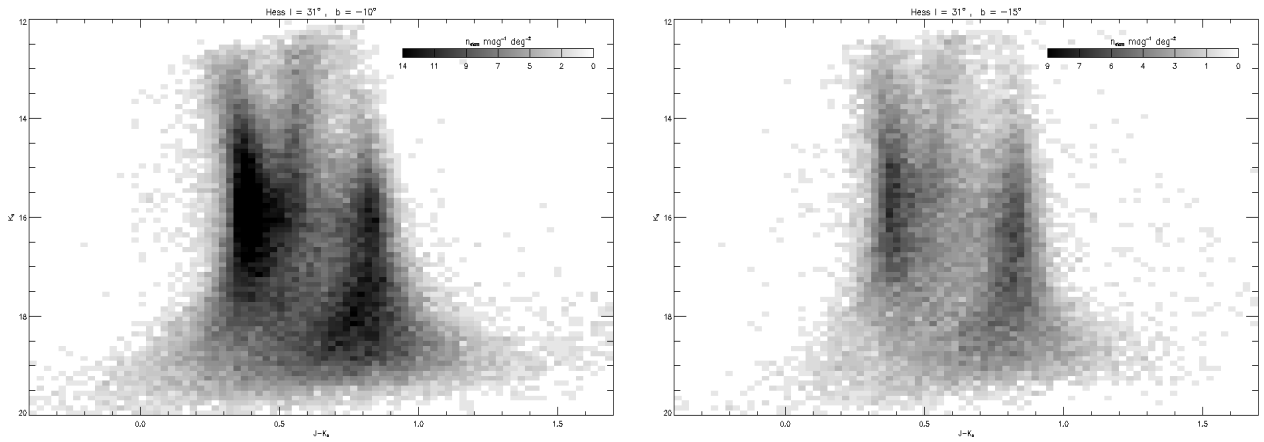

Figure 17: Hess diagrams at $l = 31°, b = -10°$ and $l = 31°, b = -15°$.

counts. For the thin disk, the position of the Sun above the Galactic plane produces a more important difference between the counts in the two hemisphere as the scale height is just 300pc.

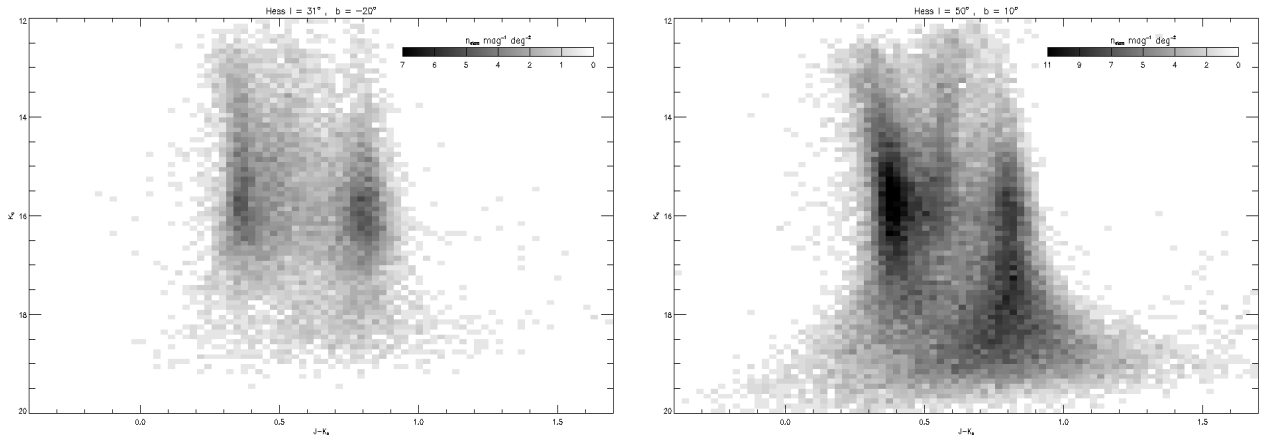

Figure 18: Hess diagrams at $l = 31°, b = -20°$ and $l = 50°, b = 10°$. We notice data is missing at faint magnitudes for the $l = 31°, b = -20°$ field.

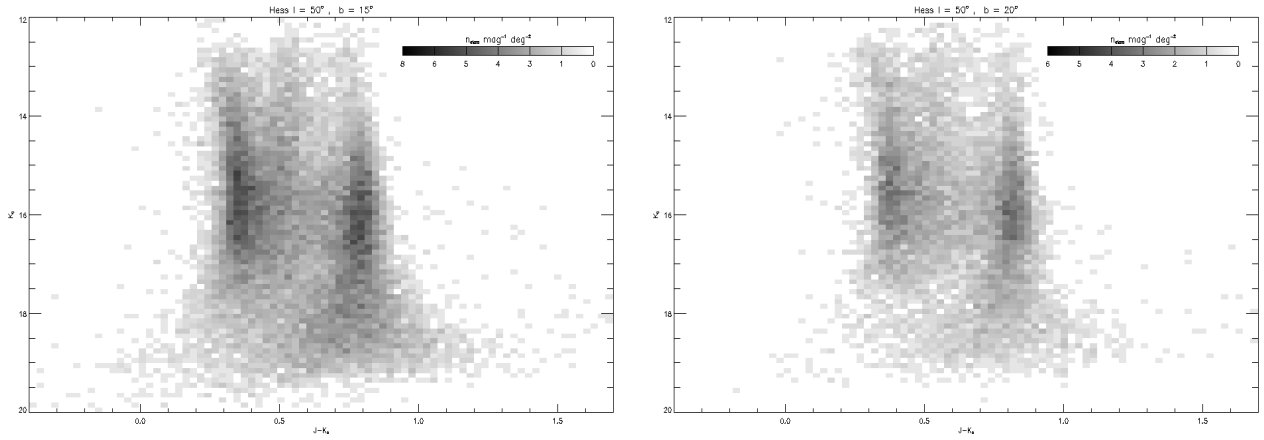

Figure 19: Hess diagrams at $l = 50°, b = 15°$ and $l = 50°, b = 20°$. Here we notice data incompleteness at $l = 50°, b = 20°$.

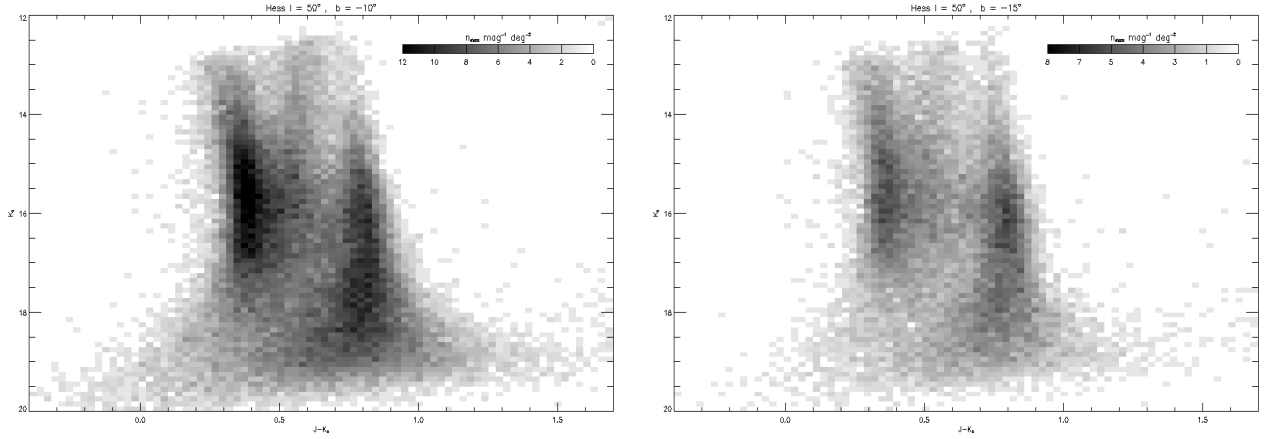

Figure 20: Hess diagrams at $l = 50°, b = -10°$ and $l = 50°, b = -15°$.

The easiest way to compare the spatial densities we see in the two hemispheres is by sub-

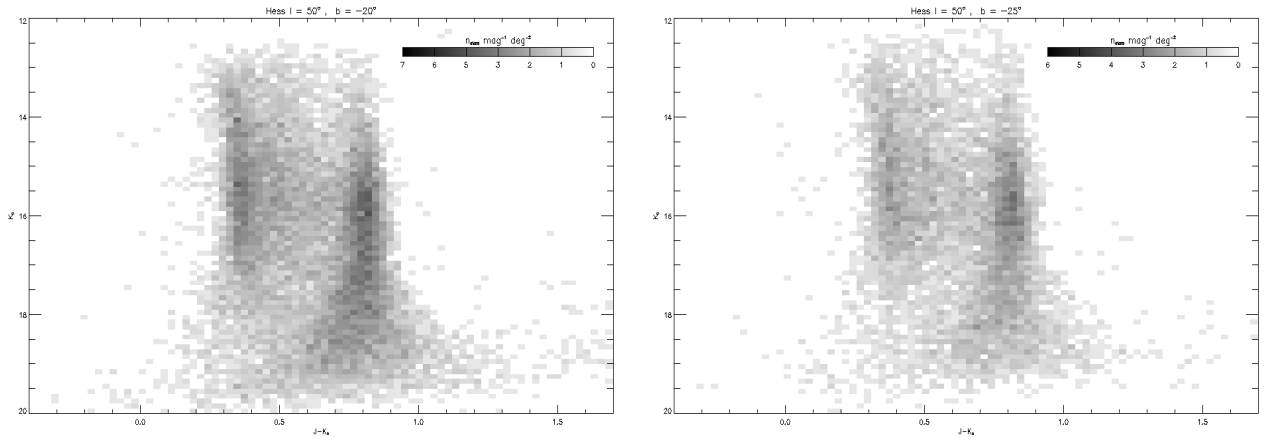

Figure 21: Hess diagrams at $l = 50°, b = -20°$ and $l = 50°, b = -20°$.

tracting them. Hess differences will reveal underdensities or overdensities. As we have noticed also in the previous section, the giant branch is an approx. symmetric structure and it disappears in hess differences. Here we will concentrate on the overdensities or underdensities we find. As predicted by the model it is not be surprising to find a general overdensity at negative latitudes, as we have already noticed performing the gaussian fit. We do not show differences between $l = 31°$ and $l = 50°$ as star counts models predict much higher N at $l = 31°$ than at $l = 50°$ so the differences do not show relevant substructures.
We show the Hess differences between the two hemispheres at both latitudes. The differences are between Hess diagrams with bins of 0.023 on colour and 0.088 mag on K magnitude.

Let us first consider the differences at $l = 31°$. The overdensity we observe in figure 23 at the negative latitudes up to K = 17 is explained by the model (figure 22) but we see and overdensity for $16.5 < K < 20$ at the positive latitude, that is not predicted by the model.

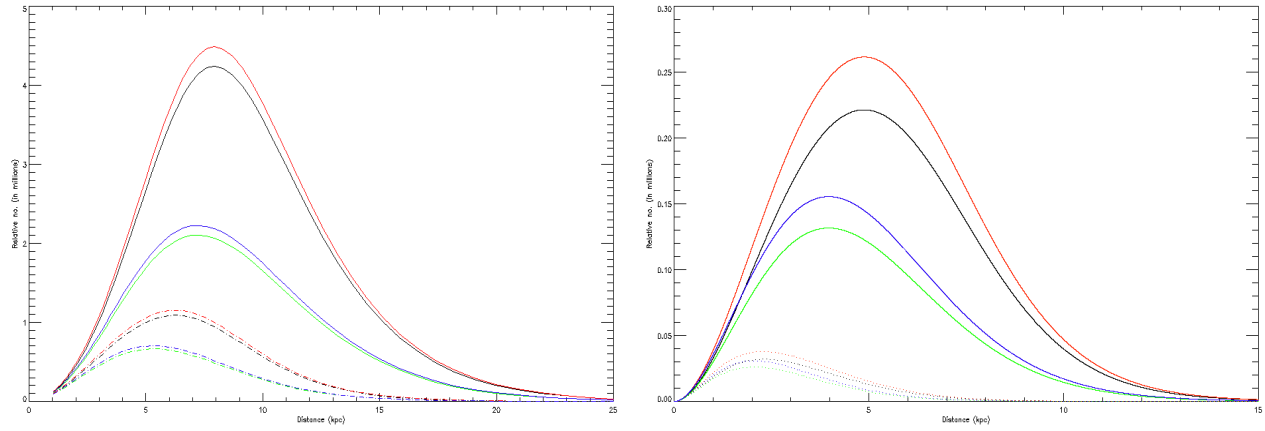

Figure 22: *left*:Star count model for the thick disk, with a scale height H = 900pc and scale length $R_0 = 3600$pc. *right*: Star count model for the thin disk, with a scale height H = 300pc and a scale length $R_0 = 2600$pc. The fact that the Sun is at a height of approx. 25 pc above the disk plane introduces an offset at negative latitudes. We show the star counts prediction at $b = 10°$ (black for $l = 31°$ and blue for $l = 50°$) and at $b = -10°$ (red for $l = 31°$ and green for $l = 50°$.) The dashed lines are the same as above but for $b = |20|$.

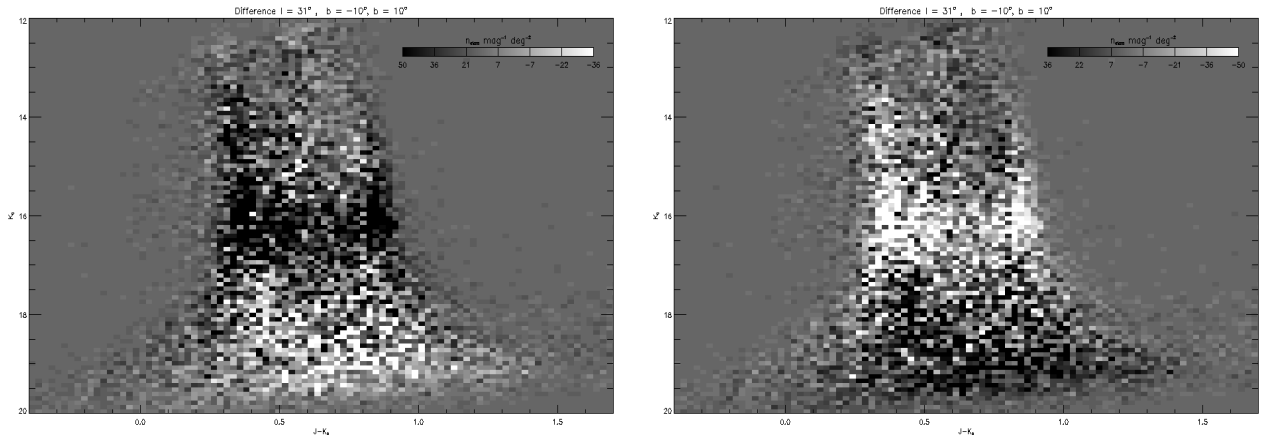

Figure 23: Hess Differences created by subtracting the star densities in the two hemispheres (difference between $l = 31°, b = -10°$ and $l = 31°, b = 10°$ in the left panel and the opposite in the right pannel) so that black (white) indicates relative overdensity (underdensity).

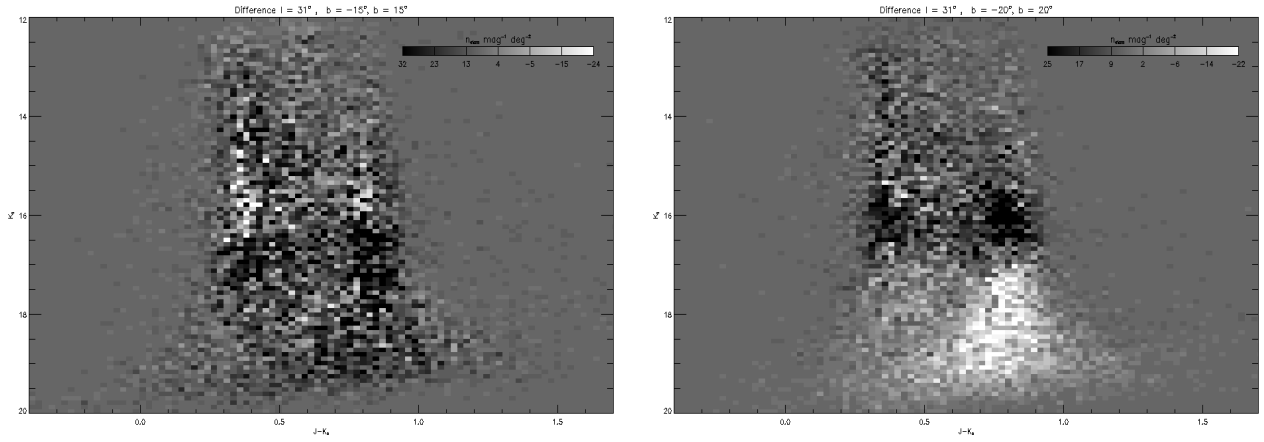

Figure 24: Hess Differences created by subtracting the star densities in the two hemispheres (difference between $l = 31°, b = -15°$ and $l = 31°, b = 15°$ in the left panel and $l = 31°, b = -20°$ and $l = 31°, b = 20°$ in the right pannel) so that black (white) indicates relative overdensity (underdensity).

If we condider that the stars in the color bin $0.7 < J - K < 0.9$ belong to the thin disk and they are scattered along the line of sight, the stars at the faint magnitudes ar the farthest. The magnitudes of these stars might be over corrected for extinction because they are not behind all the dust; moreover, we count more distant stars when looking out of the galactic plane than by looking at negative latitudes, where we count much more thin disk stars close to us. The Hess difference in figure 23 also shows an overdensity at $l = 31°, b = +10°$, in the HAC region. We show for reference (figure 27) the SDSS data which shows the main sequence stars HAC in the field $l = 30°, b = +40°$, (Belokurov et al. 2007). As we have calculated in the previous section, the overdensity observed in the SDSS data should correspond to the region $0.20 < J-K < 0.40$ and $17 < K < 20$. Thus, we think that the overdensity observed at positive latitudes in this region might be due to the presence of HAC main sequence stars.
At $l = 31°, b = |15|°$ we observe a general overdensity at negative latitudes with an overdensity at $K \approx 16$, noticing that the signal of the supposed HAC almost disappeard. The differences at $l = 31°, b = |20|°$ and $l = 50°, b = |20|°$ are not useful because, as we concluded in section 5, data

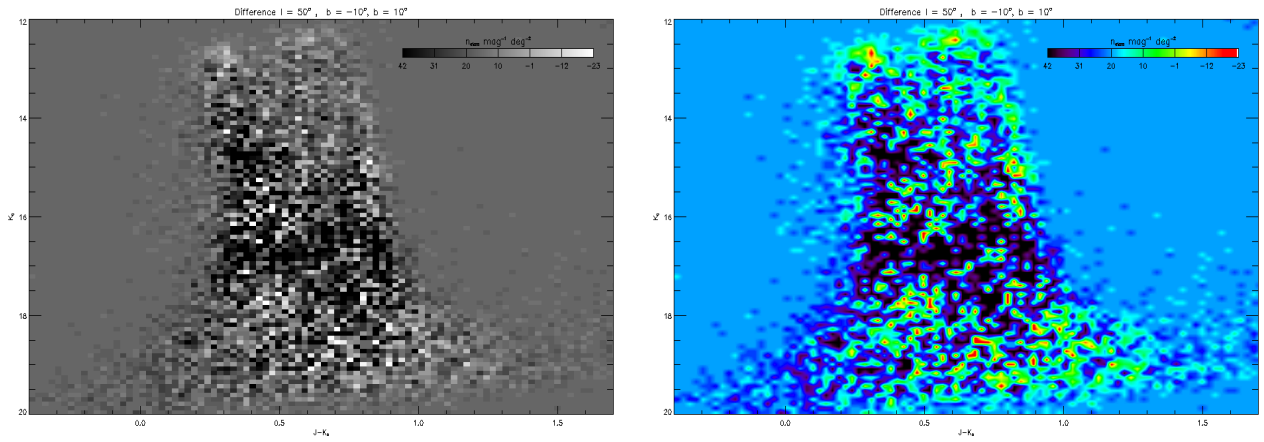

Figure 25: Hess Differences created by subtracting the star densities in the two hemispheres (difference between $l = 50°, b = -10°$ and $l = 31°, b = 10°$ in the left panel and the same in the right pannel, but in colours to evidentiate the overdensity in the HAC region) so that black (white) indicates relative overdensity (underdensity).

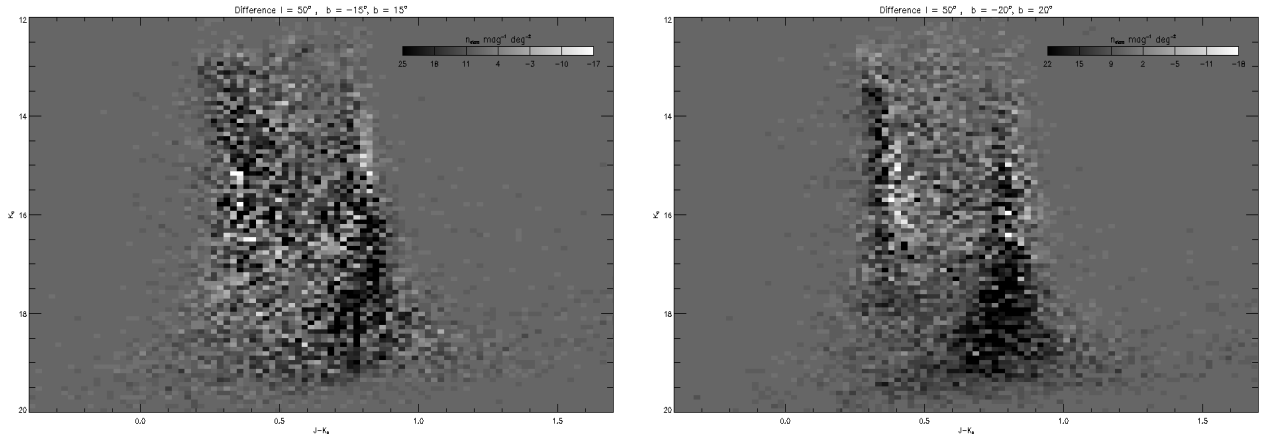

Figure 26: Hess Differences created by subtracting the star densities in the two hemispheres (difference between $l = 50°, b = -15°$ and $l = 50°, b = 15°$ in the left panel and $l = 50°, b = -20°$ and $l = 50°, b = 20°$ in the right pannel) so that black (white) indicates relative overdensity (underdensity).

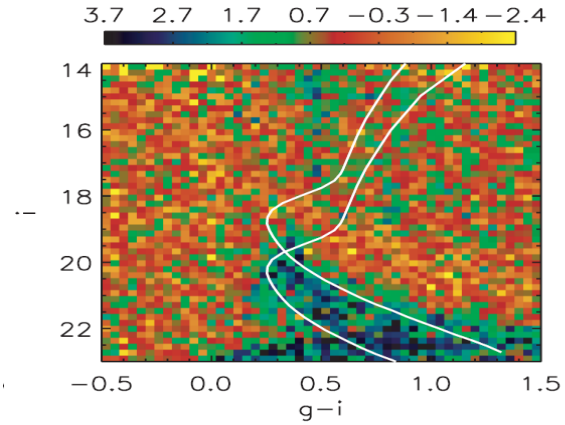

Figure 27: Difference of Hess diagrams for an on-cloud field $l = 30°, b = 40°$ and an off-cloud field $l = 15°, b = 40°$. The overdensity corresponds to upper main sequence and turn off stars in the Hercules-Aquila cloud. The white lines show M92 ridgelines shifted to distances of 10kpc and 20kpc which bracket the main sequence location. *(Belokurov et al. 2007)*

is missing at faint magnitudes in the fields $l = 31\circ, b = -20°$ (figure 18) and $l = 50°, b = 20°$ (figure 19). This explains the differences observed.
In the Hess difference at $l = 50°, b = |10|°$ in figure 25 we can again notice an overdensity in the HAC region but fainter as the total number of counts is fainter for $l = 50°$. The density of stars decreases with latitude in at both longitudes, as predicted by the model. In conclusion, there remain a few overdensities that we can not directly explain with the model but, as we are looking almost in the bulge direction, it is not so surprising that we see more variantions in star density at $l = 31°$ than at $l = 50°$, especially in the thin disk population.

6 Parameters of the thick disk

6.1 Luminosity functions

To help the interpretation of our CMDs it is useful to build luminosity functions. We divide the colours in bins of 0.1 and the K magnitudes in bins of 0.22 mag. The selection of a colour bin corresponds to the selection of stars of a certain spectral type, e.g. the bin $0.2 < J - K < 0.3$ selects FV stars (see table II). The luminosity functions will show the star densities at different apparent magnitudes, for a selected colour. We consider Poissonian errors on the density of stars.
In the next panels we show the luminosity functions for selected colours, in the $l = 31°, b = |10|°$ and $l = 50°, b = |10|°$ fields. When interpreting the luminosity functions it is useful to look at the CMDs and at the Hess differences, to see in which region of the CMD we find the different stellar densities the luminosity functions show.

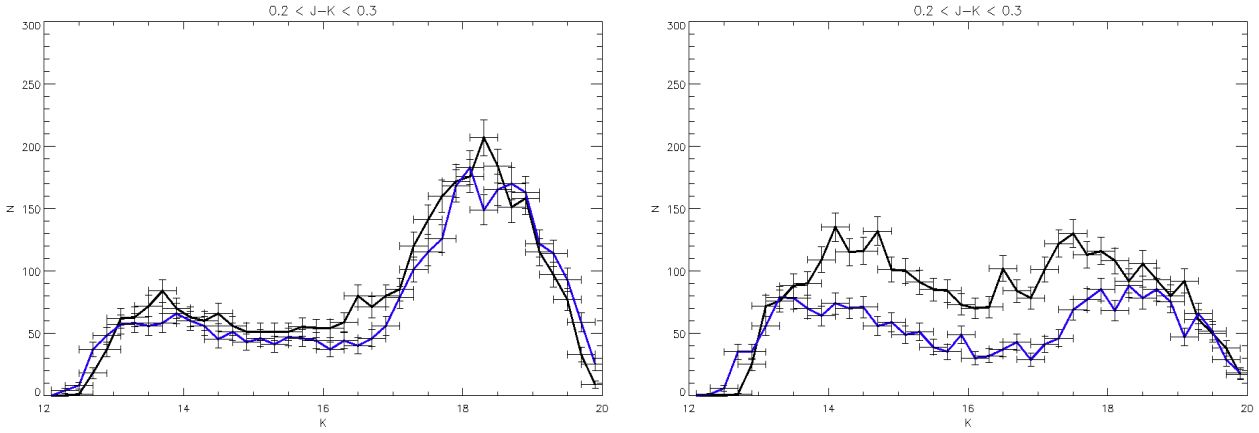

Figure 28: *left*: Luminosity functions for $l = 31°, b = 10°$ (blue) and $l = 31°, b = -10°$(black) for the $0.2 < J - K < 0.3$ color bin. If we look at the Hess diagrams we see that in this region we do not have a high star density. We notice a general overdensity of stars at $l = 31°, b = -10°$, except for faint magnitudes, where the star densities are similar. *right*: The same but for $l = 50°$. At this longitude the luminosity function shows a higher stellar density at negative b The luminosity functions have very different shapes at the two longitudes: at $l = 31°$ we can see a peak at approx. 18.5 mag while at $l = 50°$ we do not see a significant one. However, in this colour bin, the star density is not very high so the actual difference in at the two latitudes are not very big. But we notice that the luminosity functions are approx. symmetric in the two hemispheres at the same longitude, while they differ significantly if we compare the luminosity functions at the two different longitudes. The lower peak, at $K \approx 14$, is probably due to the thin disk's white dwarfs.

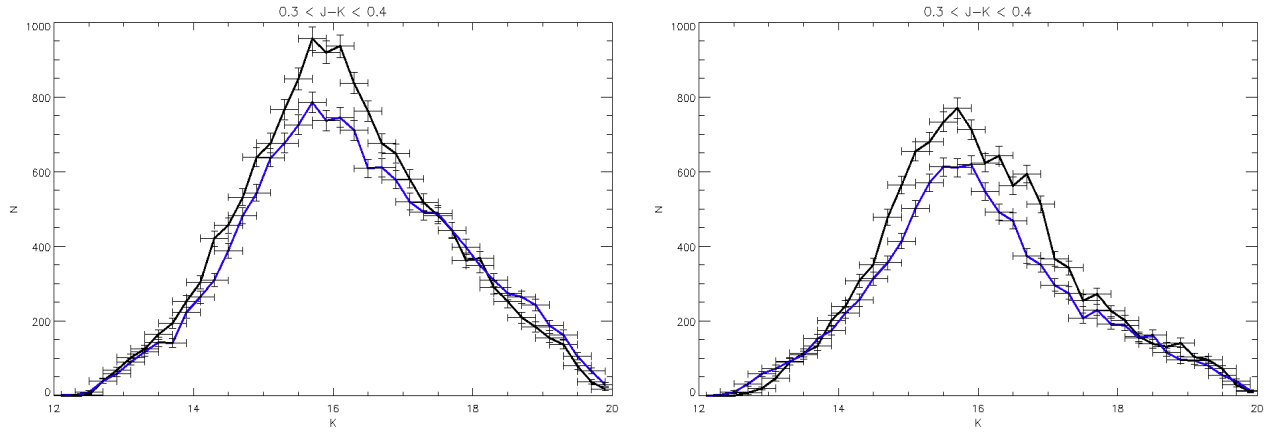

Figure 29: Luminosity functions for the $0.3 < J - K < 0.4$ colour showing the star density of thick disk main-sequence stars dispersed along the line of sight. The luminosity functions show a peak $K \approx 16$, with more counts at $l = 31^\circ$ than at $l = 50^\circ$ as predicted by the star count models. In the left panel, it is surprising that at faint magnitudes the luminosity function at $b = 10^\circ$ is almost surpassing the other one. In fig. 23 in the left panel we see a significant overdensity at $K \approx 16$ for the negative latitudes while at fainter magnitudes it disappears. We also notice that at $l = 50^\circ, b = -10^\circ$ the stellar distributions shows a very wide peak, which is not symmetric to the peak at positive latitude. At faint K magnitudes, in this color bin, the overdensity is probably due to the Hercules-Aquila cloud.

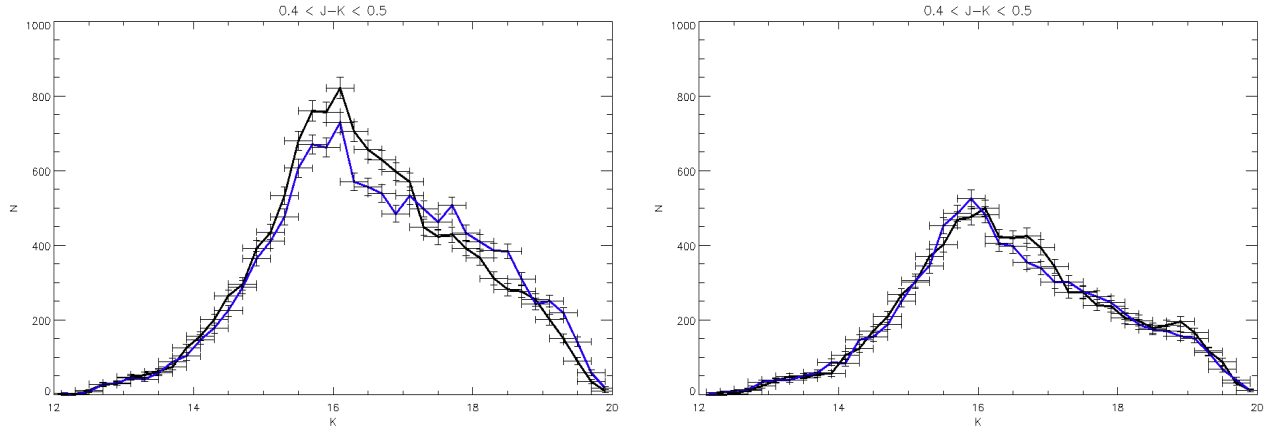

Figure 30: Luminosity functions for $0.4 < J - K < 0.5$. In this colour bin we can actually see an overdensity at positive latitudes for $l = 31^\circ, b = 10^\circ$.

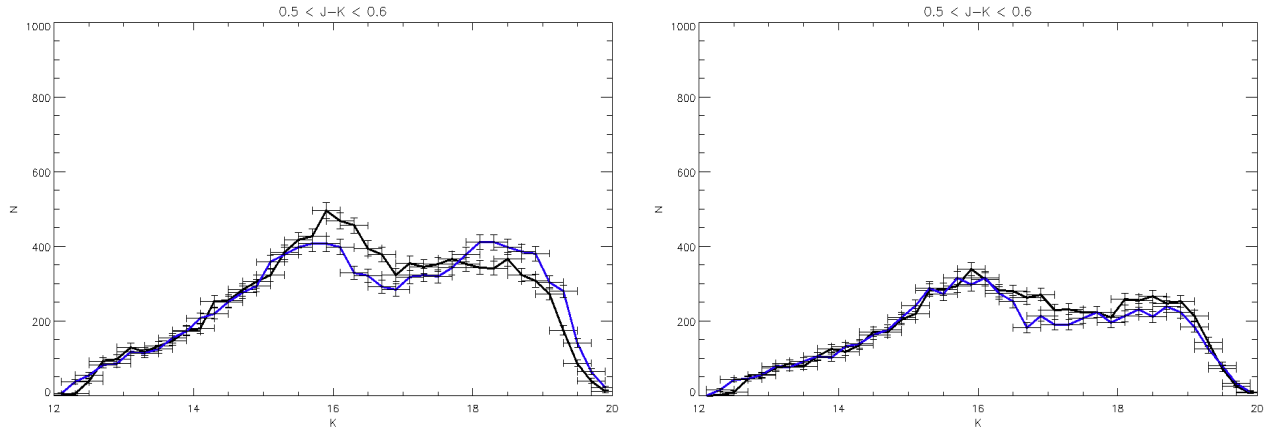

Figure 31: Luminosity functions for the $0.5 < J - K < 0.6$ colour bin. In this colour bin it becomes more clear that we have an overdensity at faint magnitudes for the $l = 31°, b = 10°$ field, which can be also noticed in the Hess difference in fig. 23 In this colour bin we are still looking at main sequence stellar densities at faint magnitudes so we do not have the problem of over-correction of the extinction. The peak at $K \approx 16$ is due to RGB stars.

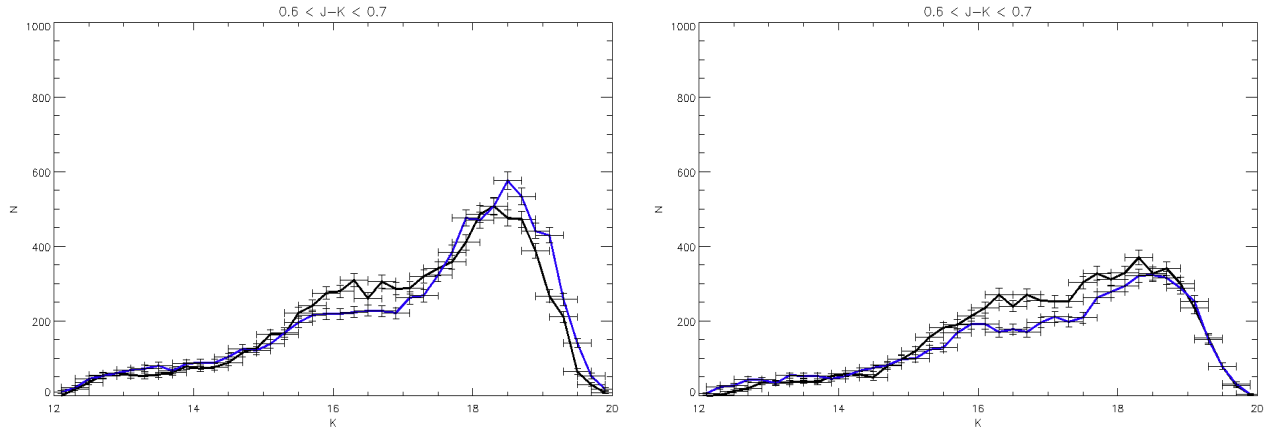

Figure 32: Luminosity functions for the $0.6 < J - K < 0.7$ colour bin. In this colour bin we start counting thin disk stars. It is possible that the K magnitudes are over-corrected for extinction.

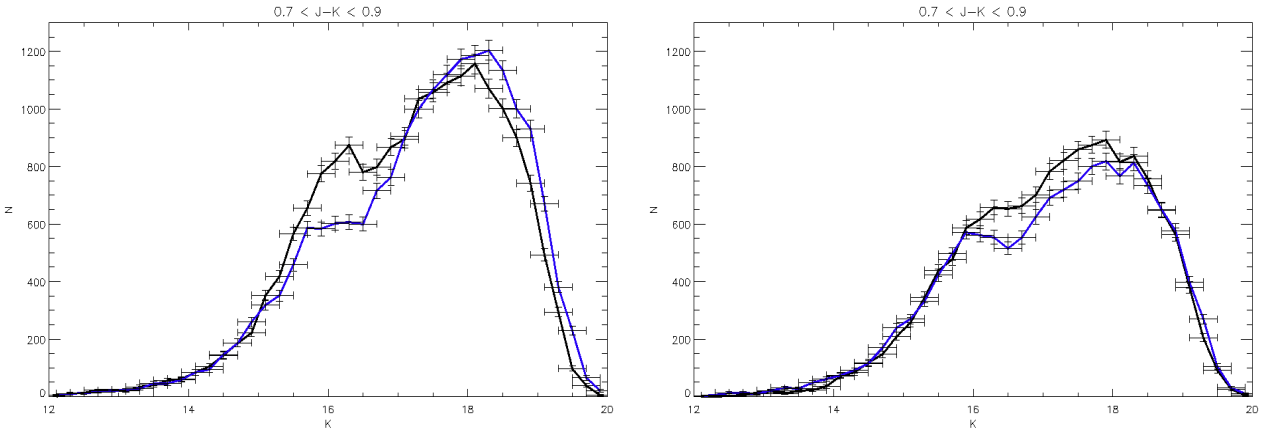

Figure 33: Luminosity functions for the $0.7 < J - K < 0.9$ colour bin. In this colour bin we find the KM stars that belong to the thin disk. We notice a peak in the luminosity function in the $l = 31°, b = -10°$ field at $K \approx 16$ mag that we cannot explain. The oposite is true at $l = 50°, b = -10°$, in the same region.

6.2 Model

Knowing that the GB stars belong to the thick disk, we now want to use them to parametrize the thick disk, finding its the scale height and the scale length.
We will use a standard star density law to describe the thin disk and thick disk populations of the Milky Way. In general, disk structures are parametrized in cylindrical coordinates by separable radial and vertical exponentials:

$$N \propto D^2 e^{-|R|/R_0} e^{-|Z+Z_\odot|/H} \tag{5}$$

where Z is the distance from the midplane, R is the planar distance from the galactic center, H_0 and R_0 are the scale height and scale length respectively and $Z_\odot$ is the height of the Sun above the Galactic plane, and we consider it to be 25pc (Juric et al, 2007 [6]). Everything is multiplied by a normalizing factor, calibrated to produce the observed local stellar density of the thick population.
For the scale height of the thick disk, star counts and models predict H = 700-1000pc and for the scale length, R_0=3-4kpc (Siegel et al. 2002). For our reference models we will adopt H_0=900pc and R_0=3600pc (The Milky Way Tomography I, Mario Juric et al 2007).
Once we know the distance D to our stars and we know (l,b), we can fully determine the three dimensional coordinates for each star:

$$\begin{aligned} X &= R_\odot - Dcos(l)cos(b) \\ Y &= -Dsin(l)cos(b) \\ Z &= Dsin(b) \end{aligned} \tag{6}$$

where for $R_\odot$, the Sun's distance from the Galactic center, we will adopt 8kpc.
We generate a set of modulus distances between 10.1 and 17.1 with a step of 0.1, from which we find a set of distances D between 1 and 26kpc (see Appendix). For each of these distances, R and Z are computed and the resulting model for the values we have chosen, R_0=3600pc and H_0=900pc ,is shown in figure 22. Now we know what we should expect.
In this section we will try to estimate H and R_0 using our data.
Considering that the stars situated along an isochrone are at the same distance, we create a polygon mask around the giant branch, as shown in figure 34. We suppose all the stars inside the mask are approximatively at the same distance.
In this section we will consider the 10 Gyrs Darthmouth isochrone with $[Fe/H] = -0.50$ and $[\alpha/Fe] = 0.20$ as it overlaps well on the GB at a modulus distance of 14.
The polygon mask is built out of the isochrone we have chosen by offsetting it in colour and magnitude. The offset we chose for the colour is 0.02 and for the magnitude is 0.2 mag. This means we are selecting stars in a $\delta d = \pm 10.5$pc range around the isochrone. We do not build the polygon mask around all the isochrone but just for a part of the giant branch, selecting stars with an absolute magnitude between M_K=0.0 mag and M_K=1.8 mag, which gives a selection of GIII stars (table III, Appendix A) with colours $0.47 < J - K < 0.55$.
Now our purpose is to calculate the star density number variation in the box, with the distance. To do so, we vary the modulus distance $K - M_{K_{GB}} = 5 \cdot log(D) - 5$ between 10, when the mask will be situated at $K \approx 12$ in our CMD and 17, when the mask will count mainly MS stars, at $K \approx 18$. We count the number of stars in the mask while offsetting the modulus distance by 0.1. In figure 34 we show the mask at a modulus dist of 14. Having fixed a range for the modulus distance we can calculate the distance of the giants directly from the modulus distance using equation:

$$D = 10^{(K - M_{K_{GB}})/5+1} pc \tag{7}$$

and the error on D is given by $\sigma_D = D/5 \cdot \delta_{(K-M_{K_{GB}})}$ while for N we consider Poissonian errors. In fig. 35 we show the star density as a function of distance for the four fields at $b = 10°$.

From fig 35 we can already calculate a rough estimate for the scale height. Neglecting the radial dependence in equation(double exp) as N varies more rapidly with the height rather than with the radial distance from the galactic center, we can obtain a relation between the distance at which the maximum occurs and the scale height:

$$\frac{\partial N}{\partial D} = 0 \tag{8}$$

$$D_{max} = \frac{2H_0}{sin(b)} \tag{9}$$

For $l = 31°, b = 10°$, D_{max} seems to be around 10kpc, from which, using the equation above, we obtain $H \approx 850$ pc which is a very good first rough estimate.
We now want to obtain a more precise estimate of the thick disk parameters, using the least

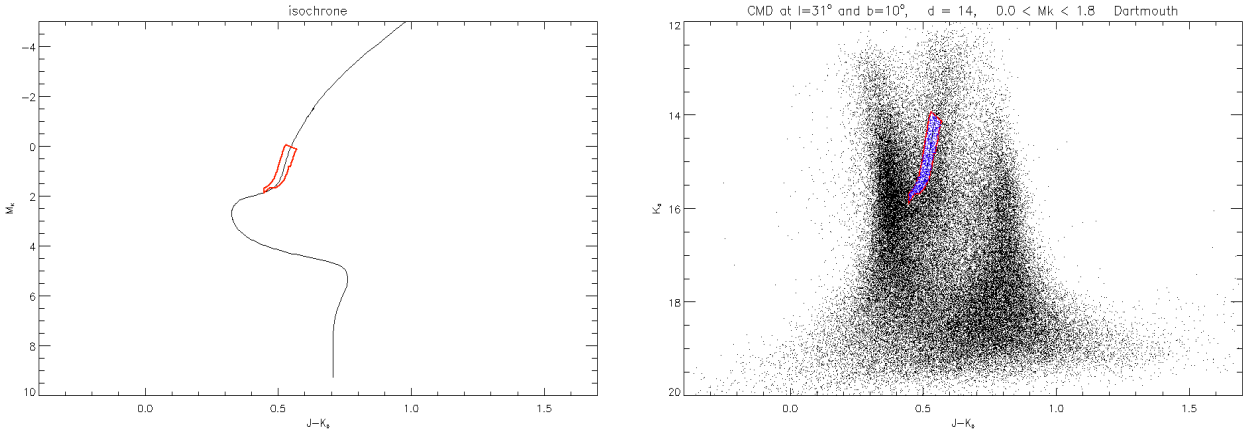

Figure 34: *left* Mask on the Dartmouth isochrone. *right* CMD and selection of stars on the giant branch with a modulus distance of 14.

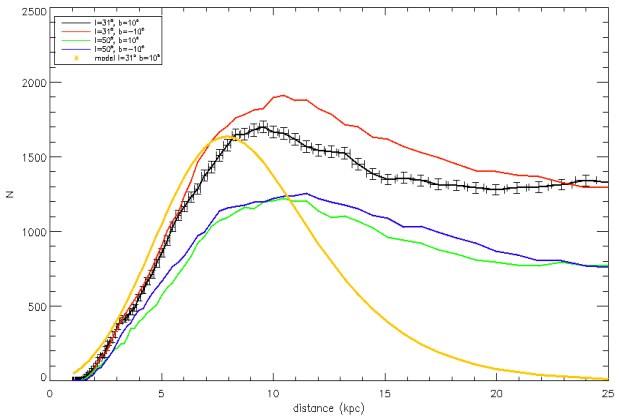

Figure 35: Star density variation with the distance for the stars counts inside the mask shown in fig. 34. The curve in yellow represents the star counts model (yellow) for H_0=900pc and $R_0 = 3600$. The density of stars we observe after the peak counts actually main-sequence stars scattered in this colour range.

squares minimisation. To do so, we need a theoretical model which we assume should fit the data. When we count the stars inside the mask at the different distances, we do not count just giants stars but also main-sequence stars that are scattered in the redder regions. We want to take into account the presence of main sequence stars in our model, knowing that they also belong to the thick disk. What we have to take into account is that these stars and GB stars are situated at a different distance from us for the same apparent magnitude K:

$$K = M_{K_{GB}} + 5log(d_{GB}) - 5$$
$$K = M_{K_{MS}} + 5log(d_{MS}) - 5$$

As the Giant Branch stars are brighter than the main sequence stars at the same magnitude, the giants are further.
If calculating the distance and its error to the giants is straightforward from the modulus distance, it is less obvious how we calculate the distance to the main sequence stars at the same magnitudes. As the creation of the polygon mask on the isochrone corresponds to selecting stars of $0.47 < J - K < 0.55$ colour, we can calculate the mean absolute magnitude of main sequence stars on the isochrone, in that range: $M_{K_{MS}} = 4.17 \pm 0.11$ mag. In order to find D_{MS} from the equations above, we need to know K which we can find from the first equation; as the modulus distance $K - M_{K_{GB}} = 5log(D_{GB}) - 5$ is given, we still need to calculate from the isochrone the mean absolute magnitude of the giants $M_{K_{GB}} = 0.94 \pm 0.8$. The error is big because the isochrone is very steep in this region, which will give us distance estimates for the main sequence stars that are affected by big errors.
The theoretical model we will try to fit our data with is:

$$F(D_{MS}, D_{GB}) = N_1 \cdot D_{GB}^2 e^{-|R_{GB}|/R_0} e^{-|Z_{GB}+Z_\odot|/H_0} + N_2 \cdot D_{MS}^2 e^{-|R_{MS}|/R_0} e^{-|Z_{MS}+Z_\odot|/H_0} \quad (10)$$

The free parameters we will obtain are N_1, R_0, H_0 and N_2, where N_1 and N_2 are just normalisation factors smaller than 1. The best estimates of our parameters minimize the sum of the weighted squared deviations between the model and the data set. The deviates between the data and the model are given by:

$$DEVIATES_i = \frac{Y_i - F_i(D_{MS}, D_{GB})}{ERR_i} \quad (11)$$

where $F(D_{MS}, D_{GB})$ is the model have we introduced above, Y_i is our data and ERR_i are the total errors on our values, taking into accout the errors on the distance and Poissonian errors on the counts. We search for R_0 and H_0 for the four fields at $b = |10|^\circ$, in the distance range 2.5-14kpc. We show the fit and the corresponding parameter values in figure 36 and table below:

$FIELD$	R_0	H_0	χ^2
$l = 31^\circ$,$b = +10^\circ$	4400 ± 1500	1100 ± 160	1.02
$l = 31^\circ$,$b = -10^\circ$	6300 ± 4600	1400 ± 460	0.94
$l = 50^\circ$,$b = +10^\circ$	4800 ± 3500	2900 ± 1000	0.90
$l = 50^\circ$,$b = -10^\circ$	4100 ± 2100	1600 ± 380	2.02

In figure 37 we show the calculated offset by the least squared method, introduced by the contamination of main sequence stars.
We know that $P(N_1, R_0, H_0, N_2) = e^{-\chi^2/2}$ is the a posteriori probability of our parameters.

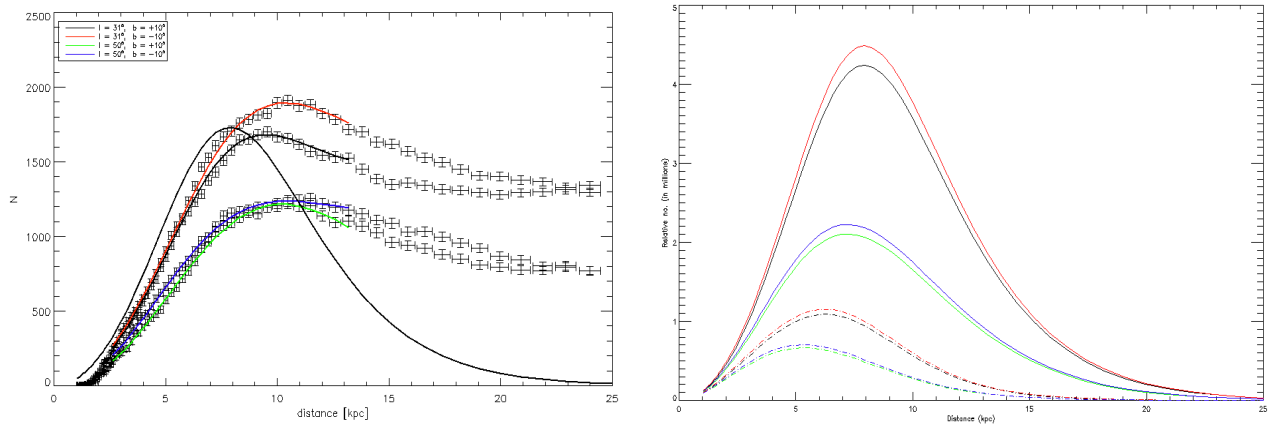

Figure 36: The interpolation curves obtained using the least squares method. In the right panel we show for reference the predicted model for the thick disk, which appears to peak at smaller distances. The values we obtain for our parameters are larger than the model values for the star counts.

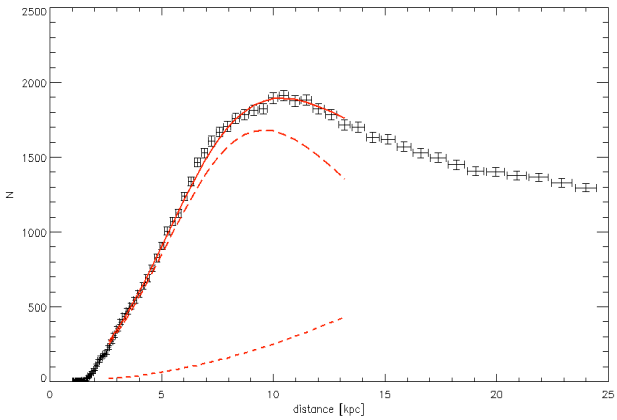

Figure 37: Interpolation for the field $l = 31°, b = -10°$. The upper dashed line shows the model and the lower dashed line shows the contamination of main-sequence stars.

When this probability is maximum (χ^2 minimum), the model best fits the data; the parameters which maximise the proability are the values we are looking for. In the panels in fig. 38 we show the χ^2 maps for two fields as a function of the two relevant parameters H and R_o in logarithmic scale.

Now that we have calculated the probability densities for the four fields, we can calculate the best estimate of our parameters by multiplying the probabilities (see fig. 39): the best estimates maximise the probability we have just obtained. To calculate the errors on the parameters we have to find the isocontour which contains 68% of the total area, by calculating the area inside the isocontours starting from the maximum probability.

For the overall estimate we have $R_0 = 5800 \pm 1100$ pc , $H_0 = 1500 \pm 160$ pc.

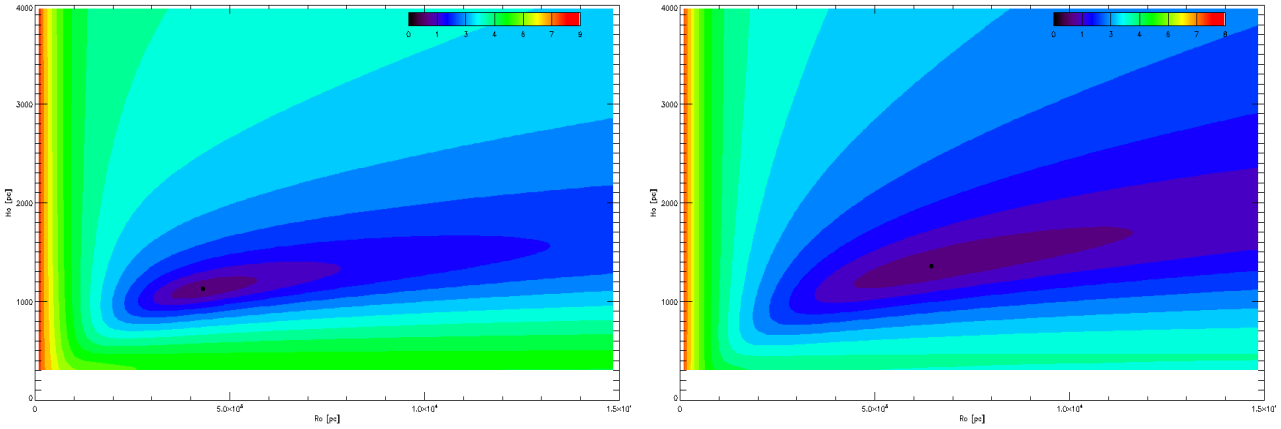

Figure 38: *left*: χ^2 in logarithmical scale for the $l = 31°$,$b = +10°$ field. The black point indicates the minimum $\chi^2 = 14.4$ to which correspond the parameters: $R_0 = 4400 \pm 1500$ and $H = 0 = 1100 \pm 160$. *right*: χ^2 in logarithmical scale for the $l = 31°$,$b = -10°$ field. The black point indicates the minimum $\chi^2 = 11.8$ to which correspond the parameters: $R_0 = 6300 \pm 4600$ and $H = 0 = 1400 \pm 460$.

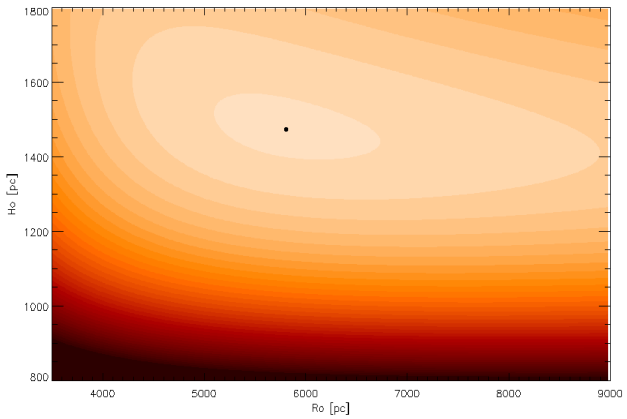

Figure 39: Total χ^2 in logarithmical scale, obtained by summing the χ^2 maps. For the overall estimate we have $R_0 = 5800 \pm 1100$ pc , $H_0 = 1500 \pm 160$ pc

7 Conclusions

The purpose of the project was to analyse the structure and content of the Hercules-Aquila cloud. For doing so, a series of JK tiles were obtained with the UKIRT telescope. As CMDs give important information about the stellar content of the fields, we have built them at all the latitudes and at the two longitudes we possess. We also built the hess diagrams and their differences for highlighting overdensities or underdensities in the two hemispheres. By matching the UKIRT stars with the DR8/SDSS stars, we were able to determine the J-K colour and K magnitude at which we should see the the Hercules Aquila cloud. We concluded that, as in this region of the CMD the errors were large and the data was partially missing, we could not complete a detailed analysis of the feature. However, the Hercules-Aquila cloud seems to be visible at $b = 10^{\circ}$ in the two longitudes $l = 31, 50^{\circ}$.
In the second part of the project we have mainly concentrated on determining the parameters of the thick disk by using the least squares minimisation method. To do so, we have used the clear signal of GB stars but we have also taken into account the contribution of main sequence stars which give an offset in the density distribution of giants. The parameters we find for the four fields have big error bars and our overall parameter estimates are $R_0 = 5800 \pm 1100$ pc , $H_0 = 1500 \pm 160$ pc. From fig. 36 we can already see that the model peaks at a lower distance than the observed peak in our distribution of stars. Knowing that neglecting the radial dependence in the stellar density model, the scale height is proportional to D_{max}, it is normal we find higher values for the disk parameters, considering the star density peaks at approx.10 kpc. In general, the parameter values we find agree with the thick disk modelisations.
The luminosity functions revealed asymmetries in the thick disk. These asymmetries could be a result of the dynamical interaction of the Thick Disk with the stellar bar (Humphreys et al. 2011). In the future, we plan to subtract the luminosity functions from the model we have obtained; the residuals will give us important information about the asymmetries and the stellar content of our populations.
As a next step we plan to integrate the star count model we have obtained on a range of distances in order to obtain a prediction of the density of GB stars in the thick disk, close to the Galactic plane.
The stellar population we observe can also be compared with stellar population model predictions such as the Besancon models and TRILEGAL. Using these models we can compute the $J - K$ vs K color magnitude diagrams for the field we need and compare the model with our data. From the comparison we can actually test the theoretical models. This work will probably result in a pubblication about the inner structure of our Galaxy in the infrared.
Analyzing the properties of the overdensities we observe in our Galaxy and their stellar content is important because they can give us important information about the history of the Milky Way. At the moment we do not know yet how many or why these overdensities exist but with the advent of upcoming surveys, such as GAIA which will survey more than a thousand million stars, we will be able to build incredibly precise three dimensional maps of the Milky Way, which will surely give us a better understanding of our Galaxy.

I plan to finish to do what I have started during the PhD. I have been accepted for a GREAT ITN position at the University of Cambridge, entitled 'Archeology of the Milky Way' and I should continue working under the supervision of Dr. Vasily Belokurov and Dr. Mike Irwin. In this PhD project we plan to continue the study of the Hercules Aquila cloud and other overdensities using the SDSS data together with the infrared data acquired with the UKIRT survey coupled with VISTA IR data and large scale ESO VLT spectroscopic survey

data. Incorporation of the Gaia distances and thus absolute luminosities for many of the stars in the Virgo overdensity and HAC will give answers as to the origin of these streams, and thus insights into the Milky Way evolution.

I am indebted to ESF for according me a 12 weeks Exchange Visit Travel Grant which allowed me to do this internship. I would like to thank my supervisor Dr. Vasily Belokurov and also Dr. Mike Irwin for their precious help and for giving me the possibility to come to the Institute of Astronomy, in Cambridge.

A Magnitudes and colours

Astronomical bodies emit radiation at multiple wavelengths. We would like to measure the complete spectral distribution of this radiation so we can determine the spectral intensity distribution, from which we measure the flux per unit frequency interval integrating over a given direction, f_ν in $Wm^{-2}s^{-1}Hz^{-1}$.
As it is difficult to calculate an absolute energy distribution because of atmosphere absorption and the response of instruments, we often calculate the integrated radiation flux just for a particular range of frequency $\delta\nu$.
We can use detectors such as CCDs to measure the apparent brightness of objects in various bands in the optical and infrared regions of the spectrum: astronomical photometry.
Instead of the calculated flux, we use magnitudes : their introduction is motivated by the fact that the response of the eye to light is essentially logarithmic in intensity. If m_1 and m_2 are the magnitudes of two stars and f_1 and f_2 their fluxes, then the following difference of magnitudes

$$m_1 - m_2 = -2.5log_{10}(\frac{f_1}{f_2}) \tag{12}$$

is called a colour. We notice it is independent on the distance.
Since the atmosphere absorbs photons and others are lost in the telescope systems and are not detected, we actually measure the flux:

$$f = \int_0^{\inf} f_\nu T_\nu F_\nu R_\nu d\nu \tag{13}$$

where T_ν is the transmission of the atmosphere, F_ν is the transmission of any filter which is used to isolate a particular range of frequencies and R_{nu} is the efficiency of the telescope system. A colour is a difference of magnitudes in two different bands. A color index measures the ratio of stellar fluxes near the effective lamba of the two bands. As it depends on the ratio of the fluxes, it is independent of the distance. The absolute magnitude M is the apparent magnitude an object would have if it were located at some distance D:

$$m - M = -2.5log(f/D) = 5log(d/D) \tag{14}$$

We usually take D=10pc, which gives us the definition of the distance modulus,

$$m - M = 5log(d) - 5. \tag{15}$$

Where d is the distance of the object.
The interstellar medium scatters light more efficiently at a short wavelength than at a long wavelength. In our CMD we will have to take into account the importance of extinction[11].
Absorption and scattering of photons in the interstellar medium cause stars to appear dimmer, so the apparent magnitude should be higher. The dimming is expressed in magnitudes:

$$m - M = 5logd - 5 + A. \tag{16}$$

B Tables

COLORS FOR MAIN-SEQUENCE STARS

ST	T_e	BC	U−V	B−V	V−R_C	V−R_J	V−I_C	V−I_J	V−J	V−H	V−K	V−L	V−M	V−N	V−[12]
B0 V	30000	−3.16	−1.38	−0.30	−0.11	−0.13	−0.26	−0.42	−0.70	−0.81	−0.93	−0.99	...	...	...
B1 V	25400	−2.70	−1.23	−0.26	−0.10	−0.11	−0.22	−0.36	−0.61	−0.71	−0.81	−0.86	...	...	...
B2 V	22000	−2.35	−1.08	−0.22	−0.09	−0.10	−0.19	−0.32	−0.55	−0.65	−0.74	−0.77	...	...	...
B3 V	18700	−1.94	−0.94	−0.19	−0.07	−0.08	−0.16	−0.27	−0.45	−0.53	−0.61	−0.63	...	...	...
B4 V	17000	−1.70	−0.84	−0.16	−0.05	−0.07	−0.13	−0.24	−0.40	−0.47	−0.55	−0.55	...	...	...
B5 V	15400	−1.46	−0.72	−0.14	−0.03	−0.06	−0.10	−0.22	−0.35	−0.41	−0.57	−0.48	...	...	...
B6 V	14000	−1.21	−0.61	−0.13	−0.03	−0.06	−0.09	−0.19	−0.32	−0.37	−0.43	−0.45	...	...	...
B7 V	13000	−1.02	−0.50	−0.11	−0.02	−0.04	−0.08	−0.17	−0.29	−0.34	−0.39	−0.42	...	...	...
B8 V	11900	−0.80	−0.40	−0.09	−0.02	−0.02	−0.15	−0.12	−0.26	−0.31	−0.35	−0.39	−0.40	...	...
B9 V	10500	−0.51	−0.17	−0.06	−0.01	0.00	−0.08	−0.06	−0.14	−0.16	−0.18	−0.20	−0.20	...	0.02
A0 V	9520	−0.30	0.00	0.00	0.00	0.02	0.00	0.00	0.00	0.00	0.00	0.00	0.00	−0.03	0.10
A1 V	9230	−0.23	0.05	0.03	0.01	0.05	0.02	0.05	0.06	0.06	0.07	0.08	0.08	0.08	0.17
A2 V	8970	−0.20	0.10	0.06	0.02	0.08	0.05	0.09	0.12	0.13	0.14	0.15	0.15	0.13	0.24
A3 V	8720	−0.17	0.15	0.09	0.03	0.11	0.08	0.13	0.18	0.21	0.22	0.23	0.23	0.20	0.31
A4 V	8460	−0.16	0.20	0.12	0.04	0.13	0.11	0.18	0.25	0.28	0.30	0.31	0.32	0.28	0.37
A5 V	8200	−0.15	0.24	0.14	0.06	0.16	0.14	0.22	0.30	0.36	0.38	0.40	0.41	0.36	0.48
A6 V	8350	−0.13	0.26	0.16	0.08	0.17	0.21	0.24	0.34	0.41	0.44	0.47	0.47	0.41	0.55
A7 V	7850	−0.12	0.28	0.19	0.10	0.19	0.27	0.28	0.39	0.47	0.50	0.53	0.53	0.46	0.60
A8 V	7580	−0.10	0.30	0.23	0.13	0.23	0.32	0.34	0.45	0.54	0.57	0.60	0.60	0.57	0.66
A9 V	7390	−0.10	0.32	0.27	0.16	0.27	0.37	0.41	0.50	0.61	0.64	0.67	0.67	0.68	0.73
F0 V	7200	−0.09	0.34	0.31	0.20	0.30	0.42	0.47	0.54	0.67	0.70	0.73	0.73	0.79	0.80
F1 V	7050	−0.10	0.36	0.33	0.22	0.32	0.44	0.51	0.58	0.73	0.76	0.79	0.79	0.86	0.91
F2 V	6890	−0.11	0.37	0.35	0.23	0.35	0.46	0.55	0.63	0.79	0.82	0.85	0.85	0.93	1.03
F3 V	6740	−0.12	0.38	0.37	0.24	0.37	0.48	0.58	0.69	0.87	0.91	0.94	0.94	0.98	1.08
F4 V	6590	−0.13	0.39	0.39	0.26	0.38	0.51	0.61	0.76	0.97	1.01	1.05	1.03	1.03	1.12
F5 V	6440	−0.14	0.40	0.42	0.27	0.40	0.54	0.64	0.83	1.06	1.10	1.14	1.13	1.07	1.16
F6 V	6360	−0.15	0.44	0.46	0.29	0.42	0.58	0.68	0.87	1.17	1.21	1.25	1.23	1.13	1.20
F7 V	6280	−0.16	0.49	0.50	0.31	0.45	0.62	0.72	0.98	1.27	1.32	1.36	1.34	1.20	1.31
F8 V	6200	−0.16	0.54	0.52	0.33	0.47	0.66	0.76	1.00	1.30	1.35	1.39	1.37	1.27	1.37
F9 V	6115	−0.17	0.59	0.55	0.34	0.48	0.69	0.79	1.03	1.33	1.38	1.43	1.40	1.31	1.47
G0 V	6030	−0.18	0.64	0.58	0.35	0.50	0.71	0.81	1.05	1.36	1.41	1.46	1.42	1.35	1.53
G1 V	5945	−0.19	0.64	0.60	0.36	0.52	0.72	0.84	1.08	1.39	1.44	1.49	1.44	1.44	1.55
G2 V	5860	−0.20	0.64	0.62	0.37	0.53	0.73	0.86	1.09	1.41	1.46	1.51	1.47	...	1.62
G3 V	5830	−0.20	0.71	0.63	0.38	0.53	0.74	0.87	1.11	1.44	1.49	1.54	1.50	...	1.85
G4 V	5800	−0.21	0.79	0.64	0.39	0.54	0.75	0.88	1.15	1.47	1.53	1.58	1.54	...	1.69
G5 V	5770	−0.21	0.86	0.66	0.39	0.54	0.76	0.89	1.16	1.52	1.58	1.63	1.59	...	1.73
G6 V	5700	−0.22	0.90	0.68	0.40	0.55	0.77	0.91	1.18	1.58	1.64	1.69	1.64	...	1.79
G7 V	5630	−0.23	0.95	0.71	0.41	0.57	0.79	0.94	1.27	1.66	1.72	1.77	1.73	...	1.85
G8 V	5520	−0.25	1.00	0.73	0.42	0.59	0.81	0.97	1.28	1.69	1.76	1.81	1.79	...	1.90
G9 V	5410	−0.28	1.13	0.78	0.44	0.61	0.83	1.01	1.30	1.73	1.80	1.86	1.87	...	1.96
K0 V	5250	−0.31	1.27	0.82	0.46	0.64	0.85	1.06	1.43	1.88	1.96	2.02	1.95	...	2.03
K1 V	5080	−0.37	1.44	0.85	0.50	0.69	0.93	1.14	1.53	2.00	2.09	2.15	2.07	...	2.20
K2 V	4900	−0.42	1.52	0.89	0.54	0.74	1.01	1.22	1.63	2.13	2.22	2.29	2.20	...	2.38
K3 V	4730	−0.50	1.80	0.97	0.58	0.83	1.08	1.35	1.79	2.33	2.42	2.51	2.39	...	2.55
K4 V	4590	−0.55	2.01	1.07	0.65	0.92	1.15	1.49	1.95	2.53	2.63	2.73	2.59	...	2.73
K5 V	4350	−0.72	2.22	1.16	0.73	0.99	1.36	1.62	2.13	2.74	2.85	2.96	2.96	...	2.91
K6 V	4205	−0.82	2.43	1.27	0.78	1.07	1.48	1.77	2.25	2.88	3.00	3.11	3.11	...	3.22
K7 V	4060	−0.92	2.64	1.38	0.84	1.15	1.60	1.93	2.37	3.03	3.16	3.27	3.27	...	3.53
M0 V	3850	−1.25	2.66	1.41	0.91	1.28	1.80	2.19	2.79	3.48	3.65	3.79	3.79	...	4.09
M1 V	3720	−1.43	2.74	1.48	0.94	1.40	1.96	2.45	3.00	3.67	3.87	4.02	4.02	...	4.32
M2 V	3580	−1.64	2.69	1.52	0.98	1.50	2.14	2.69	3.24	3.91	4.11	4.27	4.27	...	4.55
M3 V	3470	−2.03	2.65	1.55	1.10	1.60	2.47	2.94	3.78	4.40	4.65	4.85	4.85	...	5.14
M4 V	3370	−2.56	2.89	1.60	1.23	1.70	2.86	3.19	4.38	4.98	5.26	5.49	5.49	...	5.73
M5 V	3240	−3.29	3.07	1.82	1.50	1.80	3.40	3.47	5.18	5.80	6.12	6.41	6.41	...	...
M6 V	3050	−4.35	3.33	2.00	2.00	1.93	4.30	3.77	6.27	6.93	7.30	7.66	7.66	...	...

Figure 40: Table I. (S.J. Kenyon and L. Hartman, 1995)

Intrinsic Colors for Dwarfs

MK	V-I	V-K	J-H	H-K	J-K	K-L	K-L'	K-M
B8	-0.15	-0.35	-0.05	-0.035	-0.09	-0.03	-0.04	-0.05
A0	0.00	0.00	0.00	0.00	0.00	0.00	0.00	0.00
A2	0.06	0.14	0.02	0.005	0.02	0.01	0.01	0.01
A5	0.27	0.38	0.06	0.015	0.08	0.02	0.02	0.03
A7	0.24	0.50	0.09	0.025	0.11	0.03	0.03	0.03
F0	0.33	0.70	0.13	0.03	0.16	0.03	0.03	0.03
F2	0.40	0.82	0.165	0.035	0.19	0.03	0.03	0.03
F5	0.53	1.10	0.23	0.04	0.27	0.04	0.04	0.02
F7	0.62	1.32	0.285	0.045	0.34	0.04	0.04	0.02
G0	0.66	1.41	0.305	0.05	0.36	0.05	0.05	0.01
G2	0.68	1.46	0.32	0.052	0.37	0.05	0.05	0.01
G4	0.71	1.53	0.33	0.055	0.385	0.05	0.05	0.01
G6	0.75	1.64	0.37	0.06	0.43	0.05	0.05	0.00
K0	0.88	1.96	0.45	0.075	0.53	0.06	0.06	-0.01
K2	0.98	2.22	0.50	0.09	0.59	0.07	0.07	-0.02
K4	1.15	2.63	0.58	0.105	0.68	0.09	0.10	-0.04
K5	1.22	2.85	0.61	0.11	0.72	0.10	0.11	
K7	1.45	3.16	0.66	0.13	0.79	0.11	0.13	
M0	1.80	3.65	0.695	0.165	0.86	0.14	0.17	
M1	1.96	3.87	0.68	0.20	0.87	0.15	0.21	
M2	2.14	4.11	0.665	0.21	0.87	0.16	0.23	
M3	2.47	4.65	0.62	0.25	0.87	0.20	0.32	
M4	2.86	5.26	0.60	0.275	0.88	0.23	0.37	
M5	3.39	6.12	0.62	0.32	0.94	0.29	0.42	
M6	4.18	7.30	0.66	0.37	1.03	0.36	(0.48)	

Intrinsic Colors for Giants (class III)

MK	V-I	V-K	J-H	H-K	J-K	K-L	K-L'
G0	0.81	1.75	0.37	0.065	0.45	0.04	0.05
G4	0.91	2.05	0.47	0.08	0.55	0.05	0.06
G6	0.94	2.15	0.50	0.085	0.58	0.06	0.07
G8	0.94	2.16	0.50	0.085	0.58	0.06	0.07
K0	1.00	2.31	0.54	0.095	0.63	0.07	0.08
K1	1.08	2.50	0.58	0.10	0.68	0.08	0.09
K2	1.17	2.70	0.63	0.115	0.74	0.09	0.10
K3	1.36	3.00	0.68	0.14	0.82	0.10	0.12
K4	1.50	3.26	0.73	0.15	0.88	0.11	0.14
K5	1.63	3.60	0.79	0.165	0.95	0.12	0.16
M0	1.78	3.85	0.83	0.19	1.01	0.12	0.17
M1	1.90	4.05	0.85	0.205	1.05	0.13	(0.17)
M2	2.05	4.30	0.87	0.215	1.08	0.15	(0.19)
M3	2.25	4.64	0.90	0.235	1.13	0.17	(0.20)
M4	2.55	5.10	0.93	0.245	1.17	0.18	(0.21)
M5	3.05	5.96	0.95	0.285	1.23	(0.20)	(0.22)
M6		6.84	0.96	0.30	1.26		
M7		7.8	0.96	0.31	1.27		

Figure 41: [14] Tables II and III. (M.S. Bessell and J.M Brett, 1988)

C CMDs

Here we show the color-magnitude diagrams for all the fields.

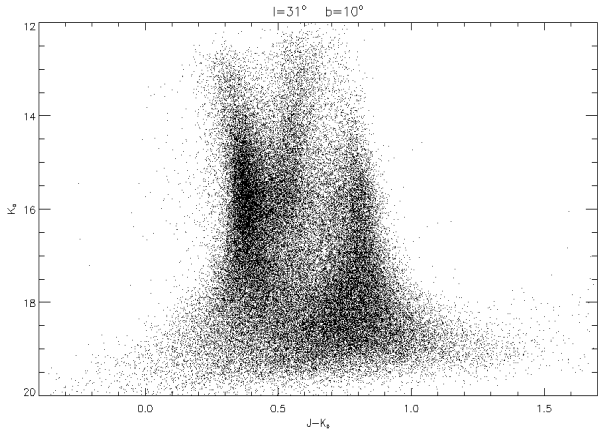

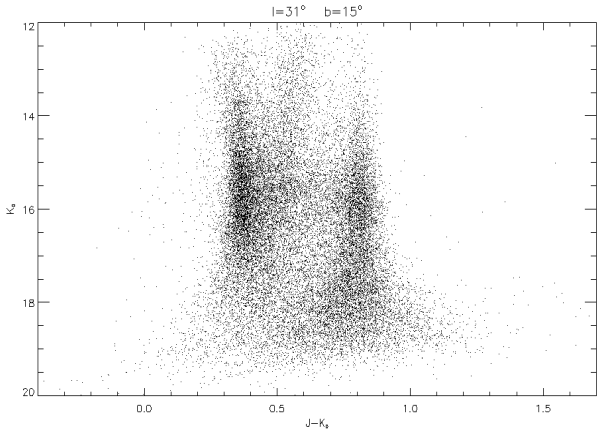

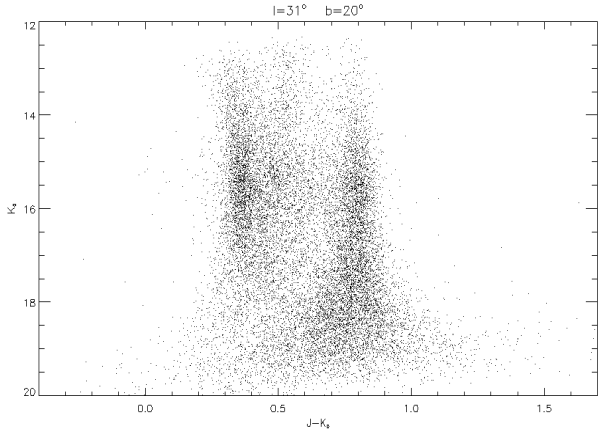

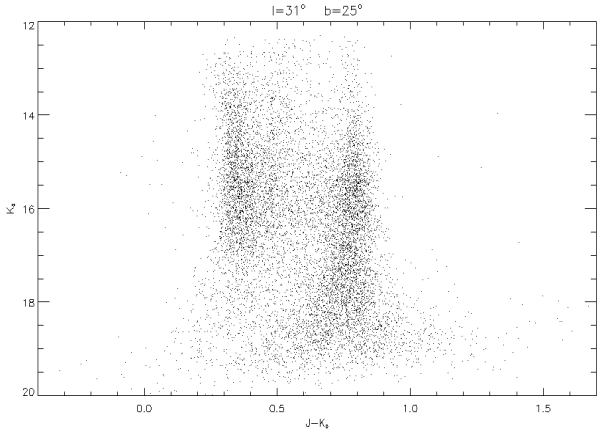

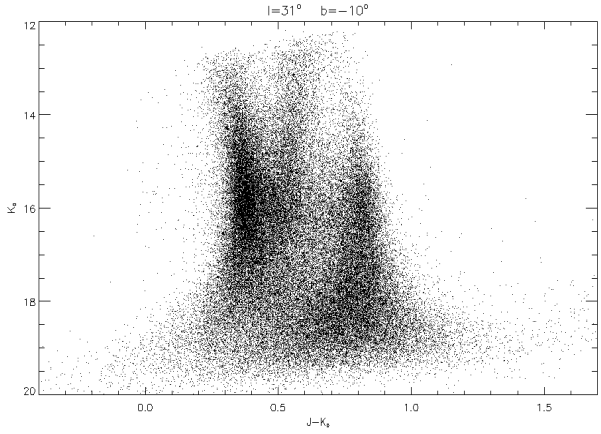

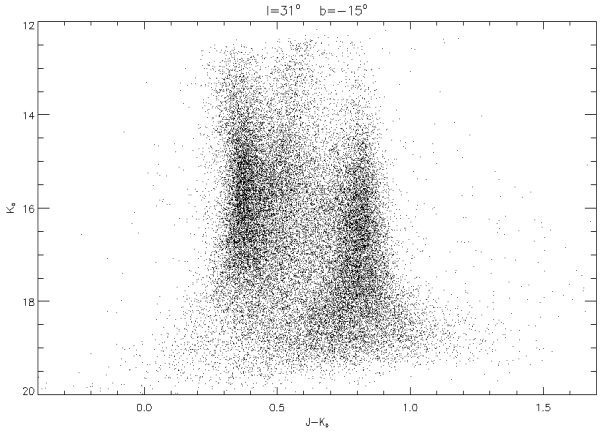

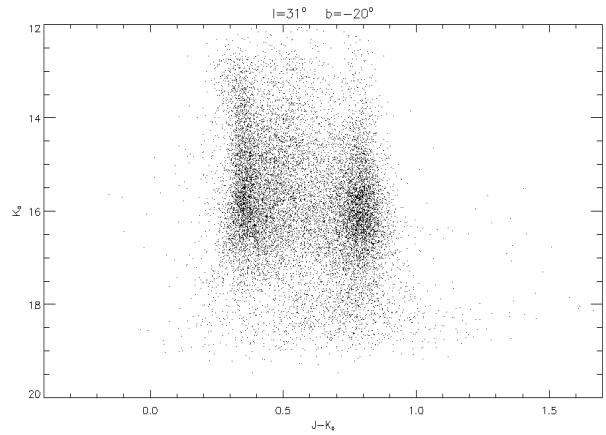
l=31° b=−20°
12
14
16
18
20
K_s
0.0
0.5
1.0
1.5
J−K$_s$

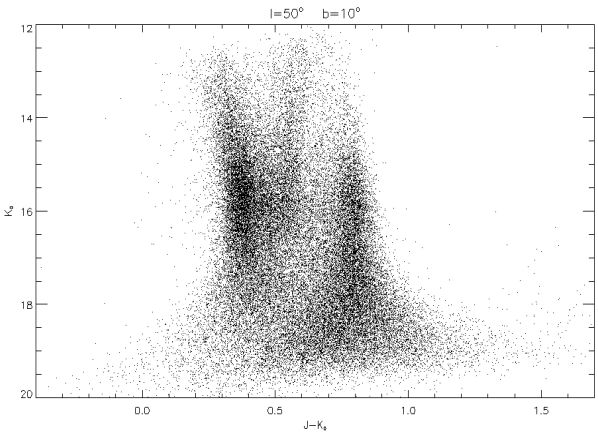
l=50° b=10°
12
14
16
18
20
K_s
0.0
0.5
1.0
1.5
J−K$_s$

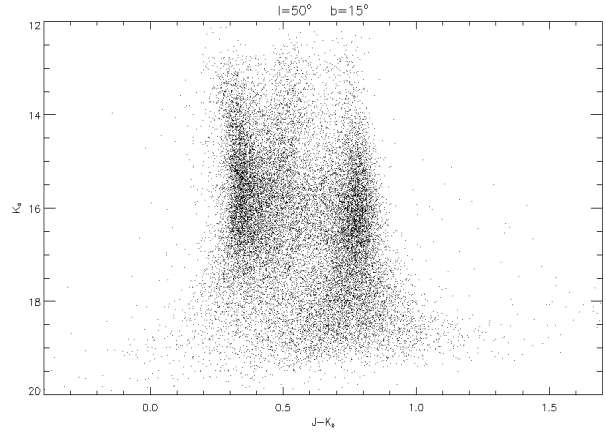
l=50° b=15°
12
14
16
18
20
K_s
0.0
0.5
1.0
1.5
J−K$_s$

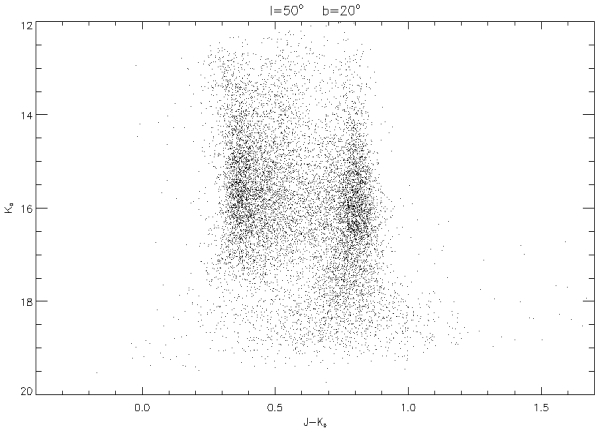
l=50° b=20°
12
14
16
18
20
K_s
0.0
0.5
1.0
1.5
J−K$_s$

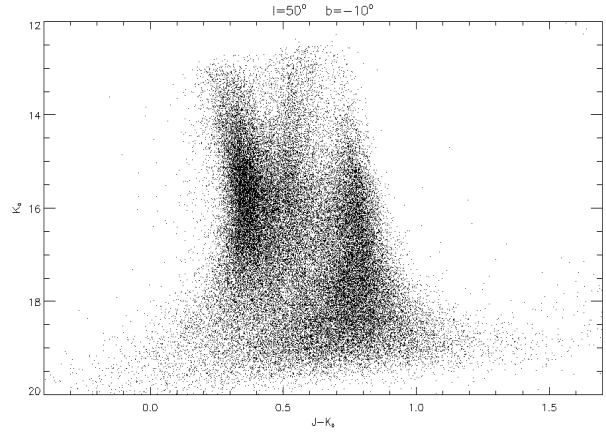
l=50° b=−10°
12
14
16
18
20
K_s
0.0
0.5
1.0
1.5
J−K$_s$

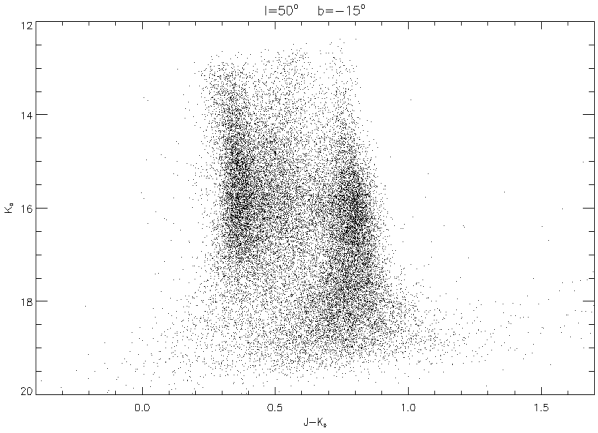
l=50° b=−15°
12
14
16
18
20
K_s
0.0
0.5
1.0
1.5
J−K$_s$

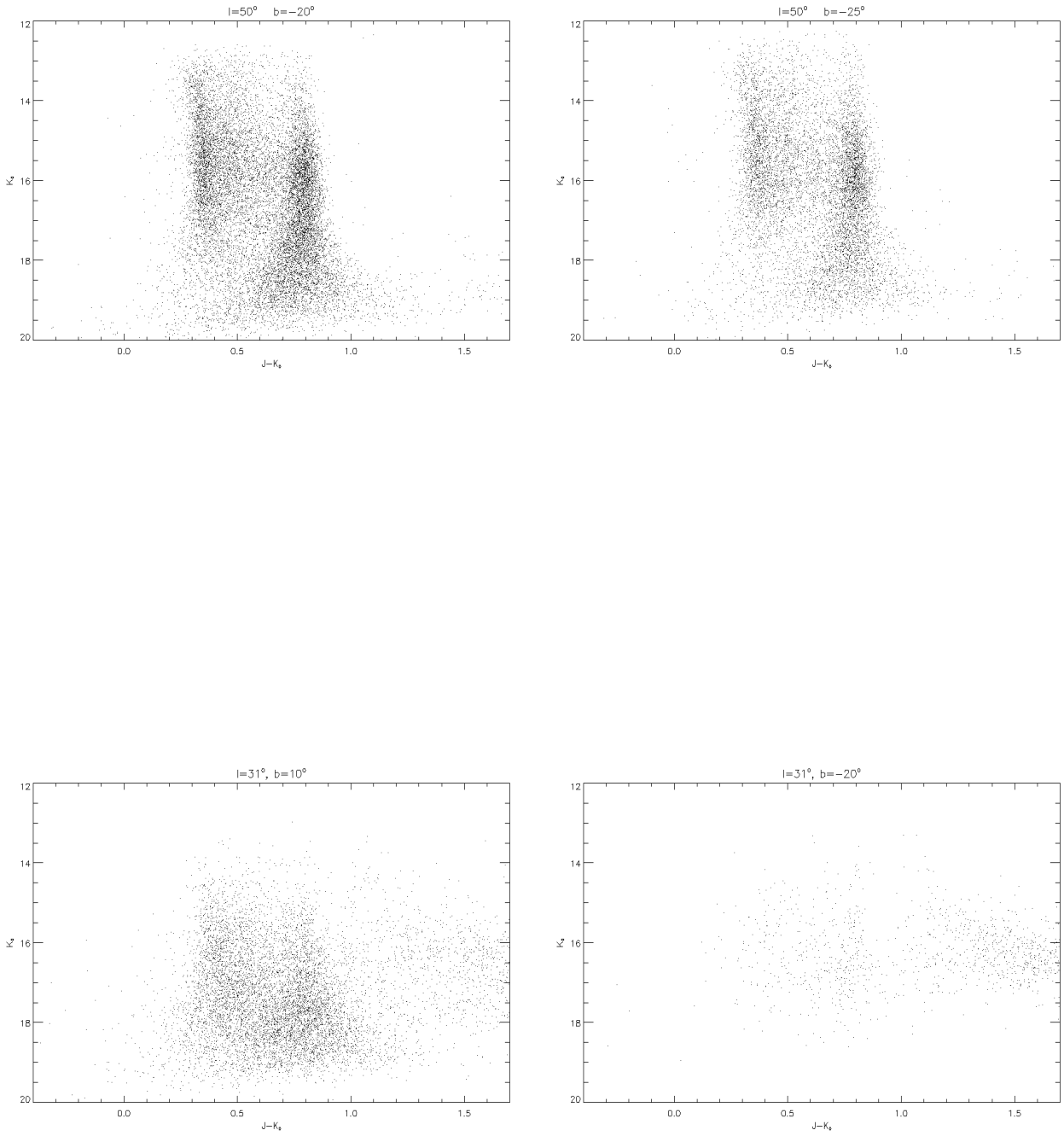

Figure 42: Non stellar objects at $l = 31°, b = 10°$ and $l = 31°, b = -20°$. We notice we do not detect objects at faint magnitudes in the second field

Bibliography

[1] Villalobos A. & Helmi A. Simulations of minor mergers. *A.J.*, 399:166–176, May 2009.

[2] Abadi M. et al. Simulations of galaxy formation in a cold dark matter universe. *A.J.*, 597:21–34, Nov 2003.

[3] Belokurov V. et al. The hercules-aquila cloud. *A.J.*, 657:L89–L92, March 2007.

[4] Belokurov V. et al. An orphan in the field of streams. *A.J.*, 658:337–344, March 2007.

[5] Gilmore G. & Wyse R. et al. Kinematics, chemistry and structure of the galaxy. *ARA & A*, 27:555–627, Nov 1989.

[6] Juric M. et al. The milky way tomography with sdss.i. stellar number density distribution. *ApJ*, 673:864–914, Feb 2008.

[7] Martin N. F. et al. A dwarf galaxy remnant in canis major: the fossil of an in-plane accretion on to the milky way. *Mon. Not. R. Astron. Soc.*, 348:12–23, Sept 2004.

[8] Newberg H. & Yanny B. et al. Sagittarius tidal debris 90 kiloparsecs from the galactic center. *A.J.*, 596:L191–L194, Oct 2003.

[9] Penarrubia J. et al. A comprehensive model for the monoceros tidal stream. *A.J.*, 626:128–144, June 2005.

[10] Rocha-Pinto H.J. et al. Exploring halo substructure with giant stars. *A.J.*, 615:732–737, Nov 2004.

[11] Schlegel D. et al. Maps of dust ir emission for use in estimation of reddening. *A.J.*, 500:525–553, June 1998.

[12] Tolstoy E. et al. Star formation histories, abundances and kinematics of dwarf galaxies in the local group. *A.J.*, 399:166–176, May 2009.

[13] Matteucci F. The evolution of alpha elements in galaxy. *S.A.I.*, 63:301–309, Mars 1992.

[14] Bessell M.S. & Brett J.M. Jhklm photometry: Standard systems, passbands and intrinsic colours. *PASP*, 100:1134–1151, Nov 1988.